Recoil polarization measurements for neutral pion electroproduction at $Q^2 = 1$ (GeV/c)^2 near the Δ resonance

J. J. Kelly,[1] O. Gayou,[2] R. E. Roché,[3] Z. Chai,[2] M. K. Jones,[4] A. J. Sarty,[5] S. Frullani,[6] K. Aniol,[7] E. J. Beise,[1] F. Benmokhtar,[8] W. Bertozzi,[2] W. U. Boeglin,[9] T. Botto,[10] E. J. Brash,[11] H. Breuer,[1] E. Brown,[12] E. Burtin,[13] J. R. Calarco,[14] C. Cavata,[13] C. C. Chang,[1] N. S. Chant,[1] J.-P. Chen,[4] M. Coman,[9] D. Crovelli,[8] R. De Leo,[6] S. Dieterich,[8] S. Escoffier,[13] K. G. Fissum,[15] V. Garde,[16] F. Garibaldi,[6] S. Georgakopoulos,[10] S. Gilad,[2] R. Gilman,[8] C. Glashausser,[8] J.-O. Hansen,[4] D. W. Higinbotham,[2] A. Hotta,[17] G. M. Huber,[11] H. Ibrahim,[18] M. Iodice,[6] C. W. de Jager,[4] X. Jiang,[8] A. Klimenko,[18] A. Kozlov,[11] G. Kumbartzki,[8] M. Kuss,[4] L. Lagamba,[6] G. Laveissière,[16] J. J. LeRose,[4] R. A. Lindgren,[19] N. Liyange,[4] G. J. Lolos,[11] R. W. Lourie,[20] D. J. Margaziotis,[7] F. Marie,[13] P. Markowitz,[9] S. McAleer,[3] D. Meekins,[3] R. Michaels,[4] B. D. Milbrath,[21] J. Mitchell,[4] J. Nappa,[8] D. Neyret,[13] C. F. Perdrisat,[22] M. Potokar,[23] V. A. Punjabi,[24] T. Pussieux,[13] R. D. Ransome,[8] P. G. Roos,[1] M. Rvachev,[2] A. Saha,[4] S. Širca,[2] R. Suleiman,[2] S. Strauch,[8] J. A. Templon,[12] L. Todor,[18] P. E. Ulmer,[18] G. M. Urciuoli,[6] L. B. Weinstein,[18] K. Wijsooriya,[25] B. Wojtsekhowski,[4] X. Zheng,[2] and L. Zhu[2]

(Jefferson Laboratory E91011 and Hall A Collaborations)

[1]*Department of Physics, University of Maryland, College Park, Maryland 20742, USA*
[2]*Massachusetts Institute of Technology, Cambridge, Massachusetts 02139, USA*
[3]*Florida State University, Tallahassee, Florida 32306, USA*
[4]*Thomas Jefferson National Accelerator Facility, Newport News, Virginia 23606, USA*
[5]*Saint Mary's University, Halifax, Nova Scotia, Canada B3H 3C3*
[6]*Istituto Nazionale di Fisica Nucleare, Sezione Sanità and Istituto Superiore di Sanità, Physics Laboratory, I-00161 Roma, Italy*
[7]*California State University, Los Angeles, Los Angeles, California 90032, USA*
[8]*Rutgers, State University of New Jersey, Piscataway, New Jersey 08854, USA*
[9]*Florida International University, Miami, Florida 33199, USA*
[10]*University of Athens, Athens, Greece*
[11]*University of Regina, Regina, Saskatchewan, Canada S4S 0A2*
[12]*University of Georgia, Athens, Georgia 30602, USA*
[13]*CEA Saclay, F-91191 Gif-sur-Yvette, France*
[14]*University of New Hampshire, Durham, New Hampshire 03824, USA*
[15]*University of Lund, Box 118, S-22100 Lund, Sweden*
[16]*Université Blaise Pascal Clermont Ferrand et CNRS/IN2P3 LPC 63, 177 Aubière Cedex, France*
[17]*University of Massachusetts, Amherst, Massachusetts 01003, USA*
[18]*Old Dominion University, Norfolk, Virginia 23529, USA*
[19]*University of Virginia, Charlottesville, Virginia 22901, USA*
[20]*Renaissance Technologies Corporation, Setauket, New York 11733, USA*
[21]*Eastern Kentucky University, Richmond, Kentucky 40475, USA*
[22]*College of William and Mary, Williamsburg, Virginia 23187, USA*
[23]*Institut Jožef Stefan, University of Ljubljana, SI-1001 Ljubljana, Slovenia*
[24]*Norfolk State University, Norfolk, Virginia 23504, USA*
[25]*University of Illinois at Urbana-Champaign, Urbana, Illinois 61801, USA*

(Received 2 September 2005; revised manuscript received 17 November 2006; published 12 February 2007)

We measured angular distributions of differential cross section, beam analyzing power, and recoil polarization for neutral pion electroproduction at $Q^2 = 1.0$ (GeV/c)^2 in 10 bins of $1.17 \leqslant W \leqslant 1.35$ GeV across the Δ resonance. A total of 16 independent response functions were extracted, of which 12 were observed for the first time. Comparisons with recent model calculations show that response functions governed by real parts of interference products are determined relatively well near the physical mass, $W = M_\Delta \approx 1.232$ GeV, but the variation among models is large for response functions governed by imaginary parts, and for both types of response functions, the variation increases rapidly with $W > M_\Delta$. We performed a multipole analysis that adjusts suitable subsets of $\ell_\pi \leqslant 2$ amplitudes with higher partial waves constrained by baseline models. This analysis provides both real and imaginary parts. The fitted multipole amplitudes are nearly model independent—there is very little sensitivity to the choice of baseline model or truncation scheme. By contrast, truncation errors in the traditional Legendre analysis of $N \to \Delta$ quadrupole ratios are not negligible. Parabolic fits to the W dependence around M_Δ for the multiple analysis gives values for $\mathrm{Re}(S_{1+}/M_{1+}) = (-6.61 \pm 0.18)\%$ and $\mathrm{Re}(E_{1+}/M_{1+}) = (-2.87 \pm 0.19)\%$ for the $p\pi^0$ channel at $W = 1.232$ GeV and $Q^2 = 1.0$ (GeV/c)^2 that are distinctly larger than those from the Legendre analysis of the same data. Similarly, the multipole analysis gives $\mathrm{Re}(S_{0+}/M_{1+}) = (+7.1 \pm 0.8)\%$ at $W = 1.232$ GeV, consistent with recent models, while the traditional Legendre analysis gives the opposite sign because its truncation errors are quite severe.

DOI: 10.1103/PhysRevC.75.025201 PACS number(s): 24.70.+s, 14.20.Gk, 13.60.Le, 13.40.Gp

I. INTRODUCTION

The electroexcitation of a nucleon resonance is described by two transverse form factors $A_{1/2}(Q^2)$ and $A_{3/2}(Q^2)$ and one longitudinal or scalar form factor $S_{1/2}(Q^2)$, where the subscript denotes the projection of the resonance spin upon the virtual photon momentum and where the dependence upon photon virtuality Q^2 describes the spatial structure of the transition. Measurement of all three transition form factors could provide stimulating tests of QCD-inspired models of baryon structure [1]. For example, one might be able to determine the admixtures of small components with mixed symmetry or orbital excitation into wave functions dominated by SU(6) symmetry. Alternatively, it has been speculated that the Roper resonance at 1440 MeV could be a hybrid baryon based upon gluonic excitation [2]. The electromagnetic transition form factors would be distinctly different for a hybrid baryon or for a radial single-quark excitation [3]. However, the electroexcitation of a resonance R by a virtual photon γ_v in a reaction of the form $\gamma_v N \to R \to Nx$, where x could be one or even several mesons, inevitably is accompanied by nonresonant contributions and is complicated by final-state interactions. Furthermore, the nucleon resonances are broad and overlapping. Therefore, measurements of differential cross sections alone are not sufficient to permit clean, model-independent determination of the multipole amplitudes for meson electroproduction or, ultimately, the transition form factors.

There has been long-standing interest in deformed components of the N and Δ wave functions [4]. The dominant amplitude for pion electroproduction at the Δ resonance is the M_{1+} amplitude, but smaller S_{1+} and E_{1+} amplitudes arise from configuration mixing within the quark core [5], often described as quadrupole deformation, from meson and gluon exchange currents between quarks [6], or from coupling to the pion cloud outside the quark core [7,8]. Thus, the quadrupole deformation is related to the ratios of isospin 3/2 electroproduction multipole amplitudes, $R_{\rm EM}^{(3/2)} = {\rm Re}(E_{1+}^{(3/2)}/M_{1+}^{(3/2)})$ and $R_{\rm SM}^{(3/2)} = {\rm Re}(S_{1+}^{(3/2)}/M_{1+}^{(3/2)})$, evaluated at $W = M_\Delta$, where $M_\Delta = 1.232$ GeV is the physical mass of the resonance. These quantities are often labeled as EMR and SMR instead, and we will use both notations interchangeably. It has been argued that the intrinsic N and Δ quadrupole moments are small [9] and that the observed EMR and SMR are dominated by nonvalence degrees of freedom.

Most previous determinations of EMR and SMR analyzed differential cross section data using Legendre expansions truncated according to the assumption of M_{1+} dominance. The data prior to 1990 generally suffered from poor statistics, limited acceptance, and relatively large systematic uncertainties, leaving even the sign of EMR at low Q^2 undetermined [10]. More recent experiments using polarized photons [11,12] now find $R_{\rm EM} \approx -2.5\%$ at $Q^2 = 0$ with relatively little model dependence [13]. Similarly, recoil polarization for parallel kinematics gave $R_{\rm SM} \approx -6.4\%$ for $Q^2 = 0.12\,({\rm GeV}/c)^2$ [14]. Furthermore, more precise measurements of the azimuthal dependence of the differential cross section give $R_{\rm SM} \approx -6.1\%$ at $Q^2 \to 0$ [15–17] and have mapped the Q^2 dependence up to $4\,({\rm GeV}/c)^2$ [18–20], but these analyses still rely upon M_{1+} dominance. However, there are several indications that this truncation may be inadequate. First, at $Q^2 \approx 0.13\,({\rm GeV}/c)^2$ there is a strong disagreement between the SMR value obtained at Bonn [21] detecting a forward pion and those obtained at MIT-Bates [15] and Mainz [14] detecting a forward proton that might be explained by an unexpectedly large S_{0+} amplitude [22]. Second, the dynamical models fail to reproduce the induced polarization for parallel kinematics at $Q^2 \lesssim 0.2\,({\rm GeV}/c)^2$ where the pion cloud is important [23,24]. Similar problems have also been observed at $Q^2 = 0.4$ and $0.65\,({\rm GeV}/c)^2$ [25]. Third, it appears to be difficult to obtain a consistent description of the real and imaginary parts of the longitudinal-transverse interference for $Q^2 \lesssim 0.25\,({\rm GeV}/c)^2$ and $W \lesssim 1.23$ GeV, where one might expect M_{1+} dominance to suffice [16,26], but a multipole analysis is not possible without more complete angular coverage and sensitivity to phases.

In principle, this model dependence can be reduced considerably by measurement of recoil and/or target polarization observables that are sensitive to the relative phase between resonant and nonresonant mechanisms [27–30]. Polarization often enhances the sensitivity to small amplitudes by interference with a large amplitude. Helicity-dependent recoil polarization is sensitive to real parts, and helicity-independent recoil polarization is sensitive to imaginary parts of products of multipole amplitudes. Furthermore, by measuring the azimuthal dependencies, one can determine response functions sensitive to the linear polarization of the virtual photon. Thus, it may be possible to perform a nearly model-independent multipole analysis if complete angular distributions are measured for a comprehensive set of recoil polarization observables. These multipole amplitudes can then be interpreted with the aid of dynamical or coupled-channels models that enforce unitary and relate the complex multipole amplitude to the real transition form factors. It is important to recognize that measurement of complex multipole amplitudes requires polarization data that are sensitive to phases; differential cross sections alone are not sufficient no matter how complete their angular coverage.

Note that coarsely binned measurements of asymmetries with respect to longitudinal target polarization have been made recently by Biselli *et al.* [31] for the $p\pi^0$ channel and by De Vita *et al.* [32] for the $n\pi^+$ channel in the resonance region with $0.35 < Q^2 < 1.5\,({\rm GeV}/c)^2$. However, those data have not been resolved into response functions and are not suitable for detailed multipole analysis.

In this paper, we report the first extensive measurements of angular distributions for recoil polarization in pion electroproduction. We have measured recoil polarization response functions for the $p(\vec{e}, e'\vec{p})\pi^0$ reaction at $Q^2 \approx 1\,({\rm GeV}/c)^2$ near the Δ resonance, obtaining angular distributions for a total of 16 independent response functions in 10 steps of W covering $1.17 \leqslant W \leqslant 1.35$ GeV; the angular coverage and statistical precision are best in the central region $1.21 \leqslant W \leqslant 1.29$ GeV. The data for $W = 1.23$ GeV were reported in Ref. [33], which focused upon the quadrupole ratios for the $N \to \Delta$ transition. Twelve of these response functions are observed here for the first time and provide rigorous tests of reaction models; none of the available models provides a uniformly accurate description of the data for previously unavailable response functions. We compare a traditional truncated Legendre analysis with a more general multipole analysis of these data. Although the two analyses are qualitatively consistent, the multipole analysis shows that truncation errors in the traditional Legendre analysis of the quadrupole ratios are not negligible.

Section II defines the response functions, Sec. III describes the experiment, and Secs. IV and V describe the cross section and polarization analyses, respectively. We compare the results with selected models in Sec. VI A and present Legendre and multipole analyses in Secs. VI B and VI C. Further discussion of the relationship between the two analyses is given in Sec. VII. Finally, Sec. VIII summarizes our conclusions.

II. RESPONSE FUNCTIONS

A. Definitions

The differential cross section for recoil polarization in the pion electroproduction reaction $p(\vec{e}, e'\vec{N})\pi$ can be expressed in the form

$$\frac{d^5\sigma}{dk_f d\Omega_e d\Omega^*} = \Gamma_\gamma \bar{\sigma}\left[1 + hA + \mathbf{\Pi}\cdot\boldsymbol{S}\right], \tag{1}$$

where $\bar{\sigma}$ is the unpolarized cross section, h the electron helicity, $\boldsymbol{S}$ the spin direction for the recoil nucleon, A the beam analyzing power, $\mathbf{\Pi} = \boldsymbol{P} + h\boldsymbol{P}'$ the recoil polarization,

$$\Gamma_\gamma = \frac{\alpha}{2\pi^2}\frac{k_f}{k_i}\frac{k_\gamma}{Q^2}\frac{1}{1-\epsilon} \tag{2}$$

the virtual photon flux for initial (final) electron momenta $k_i(k_f)$, $\epsilon = (1 + 2\frac{\mathbf{q}^2}{Q^2}\tan^2\frac{\theta_e}{2})^{-1}$ the transverse polarization of the virtual photon, θ_e the electron scattering angle, and $k_\gamma = (W^2 - m_p^2)/2m_p$ the laboratory energy a real photon would need to excite the same transition. Note that electron kinematics and solid angle $d\Omega_e$ are normally expressed in the laboratory frame, while hadron kinematics and nucleon solid angle $d\Omega^*$ are expressed in the πN center-of-mass frame. Figure 1 illustrates the kinematics of this reaction and the definitions for polarization vectors.

It is convenient to express polarization vectors in a basis where $\hat{\ell}$ is along the nucleon momentum in the c.m. frame, $\hat{n} \propto \hat{q}\wedge\hat{\ell}$ is normal to the reaction plane, and $\hat{t} = \hat{n}\wedge\hat{\ell}$. The azimuthal dependence can then be extracted, and the observables can be decomposed into kinematic factors ν_α, which depend only upon electron kinematics and response functions, $R_\alpha(x, W, Q^2)$, which carry the hadronic information, such that

$$\begin{aligned}\bar{\sigma} &= \nu_0[\nu_L R_L + \nu_T R_T + \nu_{LT} R_{LT}\sin\theta\cos\phi \\ &\quad + \nu_{TT} R_{TT}\sin^2\theta\cos 2\phi],\end{aligned} \tag{3a}$$

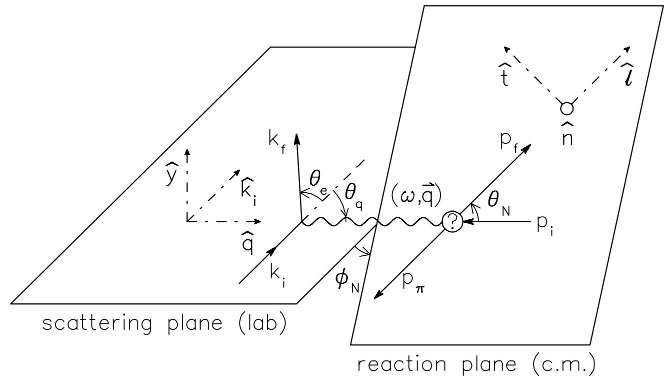

FIG. 1. Kinematics of $p(\vec{e}, e'\vec{p})\pi^0$ reaction and polarization basis vectors.

$$A\bar{\sigma} = \nu_0[\nu'_{LT} R'_{LT}\sin\theta\sin\phi], \tag{3b}$$

$$P_t\bar{\sigma} = \nu_0\left[\nu_{LT} R^t_{LT}\sin\phi + \nu_{TT} R^t_{TT}\sin\theta\sin 2\phi\right], \tag{3c}$$

$$\begin{aligned}P_n\bar{\sigma} &= \nu_0\left[\left(\nu_L R^n_L + \nu_T R^n_T\right)\sin\theta + \nu_{LT} R^n_{LT}\cos\phi \right.\\ &\quad \left. + \nu_{TT} R^n_{TT}\sin\theta\cos 2\phi\right],\end{aligned} \tag{3d}$$

$$P_\ell\bar{\sigma} = \nu_0\left[\nu_{LT} R^\ell_{LT}\sin\theta\sin\phi + \nu_{TT} R^\ell_{TT}\sin^2\theta\sin 2\phi\right], \tag{3e}$$

$$P'_t\bar{\sigma} = \nu_0\left[\nu'_{LT} R'^t_{LT}\cos\phi + \nu'_{TT} R'^t_{TT}\sin\theta\right], \tag{3f}$$

$$P'_n\bar{\sigma} = \nu_0\left[\nu'_{LT} R'^n_{LT}\sin\phi\right], \tag{3g}$$

$$P'_\ell\bar{\sigma} = \nu_0\left[\nu'_{LT} R'^\ell_{LT}\sin\theta\cos\phi + \nu'_{TT} R'^\ell_{TT}\right], \tag{3h}$$

where the response functions depend upon W, Q^2, and $x = \cos\theta$, where θ is the pion angle relative to $\vec{q}$ in the πN c.m. frame. The azimuthal angle ϕ also refers to the pion momentum. The overall factor ν_0 permits phase-space factors to be extracted from the response functions, thereby simplifying multipole expansions. This factor is usually taken as the ratio between the c.m. momentum in the final state and the c.m. momentum a real photon needs for the same transition, such that $\nu_0 = k/q_0$ where

$$k^2 = \frac{\left(W^2 + m_\pi^2 - m_p^2\right)^2}{4W^2} - m_\pi^2, \tag{4a}$$

$$q_0 = \frac{W^2 - m_p^2}{2W}. \tag{4b}$$

Regrettably, no single convention for the signs and normalizations of the response functions has gained wide acceptance. We chose

$$\nu_T = 1, \tag{5a}$$

$$\nu_{TT} = \epsilon, \tag{5b}$$

$$\nu'_{TT} = \sqrt{1-\epsilon^2}, \tag{5c}$$

$$\nu_L = \epsilon_S, \tag{5d}$$

$$\nu_{LT} = \sqrt{2\epsilon_S(1+\epsilon)}, \tag{5e}$$

$$\nu'_{LT} = \sqrt{2\epsilon_S(1-\epsilon)}, \tag{5f}$$

where

$$\epsilon_S = \frac{Q^2}{q^2}\epsilon, \tag{6}$$

and we use the azimuthal angle for the pion in Eq. (3). Note that although ϵ is invariant, ϵ_S is not and that Eq. (6) is evaluated in the πN c.m. frame. When there is insufficient information to perform a Rosenbluth separation, we employ ϵ-dependent combinations

$$\nu_T R_{L+T} = \nu_L R_L + \nu_T R_T, \tag{7a}$$
$$\nu_T R^n_{L+T} = \nu_L R^n_L + \nu_T R^n_T. \tag{7b}$$

In many of the figures to follow, we use a simplified notation to label response functions and related quantities. These labels distinguish L, T, LT, TT, and $L+T$ contributions to the unpolarized (0) cross section and to transverse (t), normal (n), and longitudinal (l) components of recoil polarization. Helicity dependence is indicated by h. For example, R_{LT} is labeled LT(0), R^n_{LT} is labeled LT(n), and R'^{ℓ}_{TT} is labeled TTh(l).

B. Legendre expansions

Legendre expansions often provide the most efficient representation of the angular dependence of a response function. Each of the response functions can be represented by a Legendre expansion of the form

$$R_\eta(x, W, Q^2) = \sum_{m=0}^{\infty} A^\eta_m(W, Q^2) P_m(x), \tag{8}$$

where η represents all of the labels needed to identify a particular response function, and $x = \cos\theta$. Notice that by extracting the leading dependencies upon $\sin\theta$, the response functions defined by Eq. (3) reduce to polynomials in x that are expected to be of low order for modest W and Q^2. This convention should also improve the accuracy of acceptance averaging within bins of x. The Legendre coefficients $A^\eta_m(W, Q^2)$ can be obtained by fitting response-function angular distributions for each (W, Q^2). Alternatively, often the most efficient method for extracting the x dependence of response functions for a particular (W, Q^2) bin is to perform a two-dimensional fit of the (x, ϕ) dependencies of the appropriate observable, cross section or polarization, with the aid of the Legendre expansion. This type of analysis can be used to extrapolate response functions to parallel or antiparallel kinematics where interesting symmetry relations have been developed but where the experimental acceptance vanishes [34,35].

III. EXPERIMENT

The experiment was performed in Hall A of the Continuous Electron Beam Accelerator Facility (CEBAF) at Jefferson Laboratory in three periods between May and August 2000 using standard equipment described in detail in Ref. [36]. Details of the design and performance of the focal-plane polarimeter (FPP) can be found in Ref. [37]. Further information specific to this experiment may be found in Refs. [38–40]. Here we summarize the salient features.

The beam energy of 4531 ± 1 MeV was measured by two independent methods and the results were in agreement. The arc method uses wire scanners to measure the beam deflection angle between the accelerator and the experimental beam lines. The eP method measures electron and proton angles for elastic scattering from hydrogen using silicon strip detectors placed symmetrically in the vertical plane of a dedicated instrument.

The beam current was monitored by a pair of resonant rf cavities that were periodically calibrated with respect to an Unser monitor. The Unser monitor is a parametric current transformer that provides absolute current measurements and is calibrated with respect to a precision current source, but it suffers from a variable offset. The rf cavities are much more stable and can be used as continuous monitors. The calibration procedure alternates between beam off and current ramping between about 10 and 100 μA in about five steps, using the beam off periods to determine the drift of the Unser offset and the current steps to determine the rf gains. This procedure was repeated several times during the experiment, with negligible differences between calibrations. The accuracy of these monitors is better than 0.5% [36].

The beam position and direction were measured by beam position monitors (BPMs) located 7.524 and 1.286 m upstream of the target. Each BPM is a four-wire antenna array tuned to the fundamental rf frequency of the beam and provides the relative position to within 100μm. The absolute positions of the BPMs are calibrated with respect to wire scanners that are surveyed regularly.

The polarized electron beam was produced by circularly polarized light from a 780 nm diode laser, pulsed at 1497 MHz, illuminating a strained gallium arsenide wafer. A Pockels cell was used to reverse the laser polarization at 30 Hz. The beam polarization was measured nearly continuously using a Compton polarimeter, with systematic uncertainties estimated to be about 1% [40]. In addition, periodic measurements were also made with a Moller polarimeter, with systematic uncertainties of about 2.4%. Statistical uncertainties were negligible for both methods. Figure 2 summarizes the polarization measurements, where the vertical dashed lines indicate movement of the laser spot needed to maintain high current.

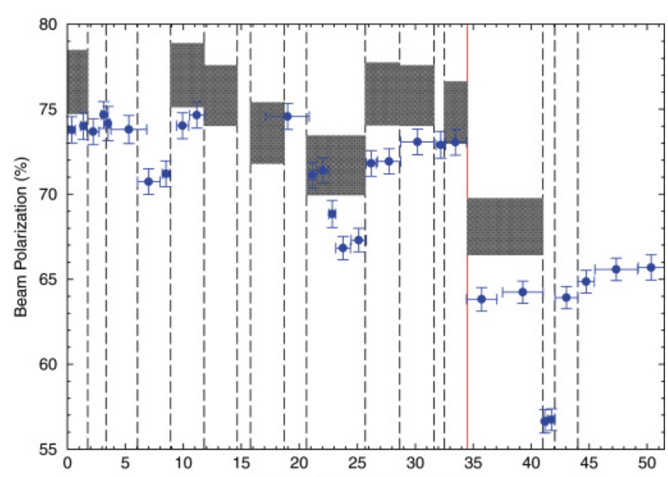

FIG. 2. (Color online) Beam polarization measurements: gray boxes indicate Moller measurements, and points Compton measurements, with systematic uncertainties included for both. Note the suppressed zero. Vertical dashed lines mark movements of the laser spot. The solid red vertical line makes the change of polarized source.

The polarization averaged about 72% for the first two running periods, but for the third it was necessary to use a different source with lower polarization, about 65%. Figure 2 shows that the time dependence of the beam polarization is minimal between spot changes. Moller results were used during the few occasions when the Compton measurements were unavailable. A comparison between the five beam polarimeters at Jefferson Lab [41] indicates that Compton measurements in Hall A are consistent with Mott measurements at the injector but that the ratio between beam polarizations obtained with the Hall A Moller and Compton polarimeters is approximately 1.034 ± 0.028, which is qualitatively consistent with the observation in Fig. 2 that the Moller results are generally about 3% larger than the Compton results. However, because the statistical precision of this ratio remains poor and relatively few runs rely on the Moller polarimeter, a correction for the relative normalization of the two polarimeters was not applied.

The production target was a cryogenic loop for liquid hydrogen operating at 19 K and 0.17 MPa with a density of 0.723 g/cm^3. The beam passes through a cylindrical aluminum cell that is 15 cm long and 6.35 cm in diameter with sidewall thickness of 178 μm and entrance and exit windows approximately 71 and 102 μm thick, respectively. To avoid damage to the target cell and to minimize luminosity variations due to local heating or boiling, the beam was rastered over a 4×4 mm^2 pattern. Measurements of rates versus current demonstrate that the average target density decreases by less than 2% for rastered currents in the range 20–60 μA relevant to the cross section measurements [39]. Furthermore, the electron singles rate provided a continuous luminosity monitor because the electron spectrometer remained fixed throughout the experiment.

Additional data were taken with about 5 μA of unrastered beam on a thin carbon foil and on dummy targets consisting of aluminum foils separated by 4, 10, or 15 cm that mimic the windows of a cryogenic cell. These data were used to determine the mispointing of the spectrometers, and the data for the 15 cm dummy cell were used to determine the contribution of the cell walls for the production data.

Particles were detected by a pair of high-resolution QQDQ spectrometers of identical design, with electrons observed in the left and protons in the right spectrometer. These spectrometers have a central bend angle of 45° and nominal acceptances of $\pm 4.5\%$ in momentum, ± 60 mr in vertical angle, and ± 30 mr in horizontal angle. The cross section data taken during the first of three running periods were taken with 80 mm tungsten collimators at distances of 1.109 m for the left or 1.100 m for the right with nominal apertures of 6 msr. Polarization data taken in the next two running periods were acquired with open apertures. The entrance windows were 178 μm Kapton while the exit windows were 100 μm titanium.

The position of the electron spectrometer was determined by survey. The initial position of the proton spectrometer was also determined by survey for each run period, and subsequent angles were measured using accurately placed floor marks observed through a closed-circuit television camera mounted on a linear translation stage without parallax. These raw angle measurements were then corrected for roll and pitch as measured by bi-axial inclinometers. However, because the spectrometers do not rotate about a fixed pivot, it is necessary to correct for possible mispointing. Corrections for mispointing were deduced from scattering data for the carbon target. The spectrometer offsets deduced for the electron arm, which was stationary for each run period, were consistent with constant values that were less than 2 mm and consistent with survey. The offsets for the hadron arm varied between about -4 and $+1.5$ mm with the motion of the spectrometer, but were reproducible without motion [38].

Both arms use two vertical drift chambers (VDCs) for tracking that are inclined by $\pm 45^\circ$ with respect to the central trajectory and are separated by 50 cm. Each chamber contains two planes of sense wires inclined at $\pm 45^\circ$ with respect to the midplane (uv configuration). Valid tracks typically produce signals on three to five sense wires. These detectors typically provide intrinsic resolutions of $\sigma_{x,y} = 100$ μm for positions and $\sigma_{\theta,\phi} = 0.5$ mrad for angles. Further details about the VDCs are provided in Ref. [42].

Both arms also use two trigger planes, S1 and S2, consisting of six plastic scintillator paddles that are 5 mm thick, overlap by about 0.5 cm, and are viewed by photomultiplier tubes (PMTs) on both ends. Five types of trigger were produced by the trigger supervisor module using signals from the two trigger planes in each spectrometer. A T1 (T3) trigger in the electron (proton) arm requires coincidence between paddle i of S1 and paddle j of S2 with $|i - j| \leqslant 1$, with PMT signals above threshold in both ends of both paddles. A T2 (T4) trigger in the electron (proton) arm misses one or more of the PMT signals or fails the directivity requirement. The T5 primary coincidence trigger requires T1 and T3 within 100 ns of each other, where T3 and T4 include adjustable delays depending upon hadron momentum. The time resolution for the coincidence trigger is typically about $\sigma = 0.3$ ns. Events corresponding to any of these triggers can be recorded, but triggers other than T5 were generally prescaled to limit computer dead time.

A simple cut on flight time between scintillator planes was sufficient to identify electrons. For the first running period, a single large scintillator paddle, labeled S0, was included in the proton trigger. After the first running period, the S0 scintillator was replaced with an aerogel Cerenkov detector with $n = 1.025$, and the aerogel signal was used in the proton trigger to suppress pion background with momentum greater than 0.63 GeV/c. We could then make polarization measurements at forward angles with higher beam currents without excessive dead time.

Recoil polarization measurements were made using the focal plane polarimeter (FPP) installed in the proton arm. More complete details of the construction and operation of the FPP can be found in Refs. [36,37]. The FPP consists of two front straw chambers, a carbon analyzer of adjustable thickness, and two rear straw chambers. The front chambers were separated by 114 cm, and each contains six planes in a $vvvuuu$ configuration. The rear chambers were separated by 38 cm. Chamber 3 has a $uuvvxx$ and chamber 4 a $uuuvvv$ configuration, where x denotes sensitivity to the dispersive direction. The analyzer consisted of five graphite plates with thicknesses of 1.9, 3.8, 7.6, 15.2, and 22.9 cm separated by about 1.6 cm that can be deployed in any combination to optimize the analyzing power for specified proton momentum.

TABLE I. Settings for the proton spectrometer. Here θ_p is the laboratory angle with respect to the beam, p_p is the central momentum, and θ_{pq} is the c.m. angle with respect to $\vec{q}$. The fifth column lists the ^{12}C thickness used for the FPP, and the final column lists the nominal precession angle for the central momentum.

θ_{pq} (deg)	θ_p (deg)	p_p (GeV/c)	charge (Coulomb)	^{12}C thickness (cm)	χ_0 (deg)
0	42.31	1.378	25.9	49.5	143.3
25	38.12	1.350	7.9	49.5	141.3
−25	46.33	1.350	4.6	49.5	
50	34.29	1.270	18.9	34.3	135.7
−50	50.18	1.270	12.9	34.3	
90	29.81	1.066	15.5	22.9	122.1
−90	54.79	1.066	20.1	22.9	
135	30.81	0.819	14.6	11.4	107.1
−135	53.64	0.819	27.6	11.4	
155	34.71	0.742	13.9	11.4	102.8
−155	49.72	0.742	13.6	11.4	
180	42.28	0.703	5.0	7.6	100.8

Spectrometer settings were chosen to obtain $(W, Q^2) = [1.232 \text{ GeV}, 1.0\,(\text{GeV}/c)^2]$ for a nominal beam energy of 4.535 GeV. Thus, the electron spectrometer remained fixed at 14.095° with a central momentum of 3.660 GeV/c. The nominal settings for the proton spectrometer, with accumulated charge, are summarized in Table I. It is convenient to define θ_{pq} as the nominal center-of-mass angle between the nucleon momentum and the momentum transfer in the laboratory frame with positive (negative) sign corresponding to forward (backward) angles with respect to the beam direction. The experiment was divided into three periods. The first period was used to scan the angular distribution and to obtain differential cross sections for all settings except $\theta_{pq} = 180^\circ$ using the 6 msr collimator in the hadron arm and relatively low currents to limit dead time. The second and third periods used the highest possible currents to obtain adequate statistics for recoil polarization and used the aerogel detector for forward angles to suppress dead time due to accidental π^+ coincidences.

IV. CROSS SECTION ANALYSIS

A. Acceptance

In each spectrometer, a track is defined by the four reconstructed target variables $(\delta, y, \theta, \phi)_{\text{tgt}}$; these variables are defined according to TRANSPORT [43] conventions. Rather than attempt to visualize the four-dimensional volumes populated by event coordinates for each spectrometer, one normally inspects two-dimensional projections. An event that is safely near the center of the distribution in one projection may be found near the edge of another where either the experimental acceptance or the calibration of the magnetic optics may be suboptimal. Therefore, it is useful to construct a measure R_{eh} of the distance between event coordinates and the boundary of a multidimensional acceptance volume that is based upon two-dimensional projections that are more amenable to visualization. We employ a variation of the R-function method that was originally developed by V. Rvachev [44,45] and applied to $(e, e'p)$ reactions by M. Rvachev [46,47]. Further details of our implementation may be found in [39].

B. Simulation

The differential cross sections for each kinematic bin were obtained from comparison between experimental and simulated yields. The simulations used MCEEP [48] to apply radiative corrections to a theoretical model, resulting in a six-fold differential cross section, and to integrate the theoretical cross section over the experimental acceptance. MCEEP samples the phase space uniformly, over a volume larger than the experimental acceptance, and evaluates the yield

$$Y_i = \mathcal{L} \int \mathcal{K}_i d^6\sigma \otimes \mathcal{R}, \tag{9}$$

where $\mathcal{L}$ is the luminosity, $\mathcal{K}_i$ represents the acceptance function for bin i, $d^6\sigma$ represents the model cross section for each event, $\otimes$ represents convolution, and $\mathcal{R}$ represents resolution functions for quantities measured in the focal plane. Here $\mathcal{K}_i = 1$, if $R_{eh} > R_{\text{cut}}$ or 0 otherwise based upon target variables that are reconstructed from focal-plane coordinates convoluted with resolution functions.

The model cross section was based upon tabulated multipole amplitudes for MAID2000 [49]. The kinematics for each event were used to interpolate the multipole amplitudes with respect to (W, Q^2) and then to compute the five-fold differential cross section in the laboratory frame.

The radiative corrections include bremsstrahlung in the target before and after scattering, internal soft-photon processes according to the Schwinger prescription, and radiation of hard photons using the Borie-Drechsel [50] prescription with the peaking approximation. Multiple scattering within the target and windows is included also. These corrections do not account for polarization effects. Further details can be found in Refs. [39,48].

Figure 3 shows that the simulation reproduces the distributions for reaction kinematics very well. Note that the experimental acceptance function R_{eh} is shown without applying the cut. The optimal choice for R_{cut} is somewhere below the center of the plateau in the ratio between experimental and simulated yields. The systematic uncertainty due to the acceptance function, estimated from the flatness of the plateau, varies between 0.6% and 2.4%.

The missing mass for this reaction is quite sensitive to laboratory angles; for example, at $\theta_{pq} = -155^\circ$ the sensitivity to electron angle is 13 MeV/degree for our kinematics. Thus, comparing the simulation with data for $\theta_{pq} = -155^\circ$ we adjusted the electron angle by -0.05°, which is well within the survey uncertainty, and then find good agreement with the missing mass peaks for all other settings as well. Furthermore, the width of the missing mass peak is underestimated by the simulation unless resolution functions are applied to the track coordinates. We found that Gaussian resolutions with $\sigma = 0.5$ mm applied to the hit positions in each VDC plane provide good agreement with those widths. This simple expedient compensates for deficiencies in the simulation of multiple scattering, magnetic optics, and/or event reconstruction.

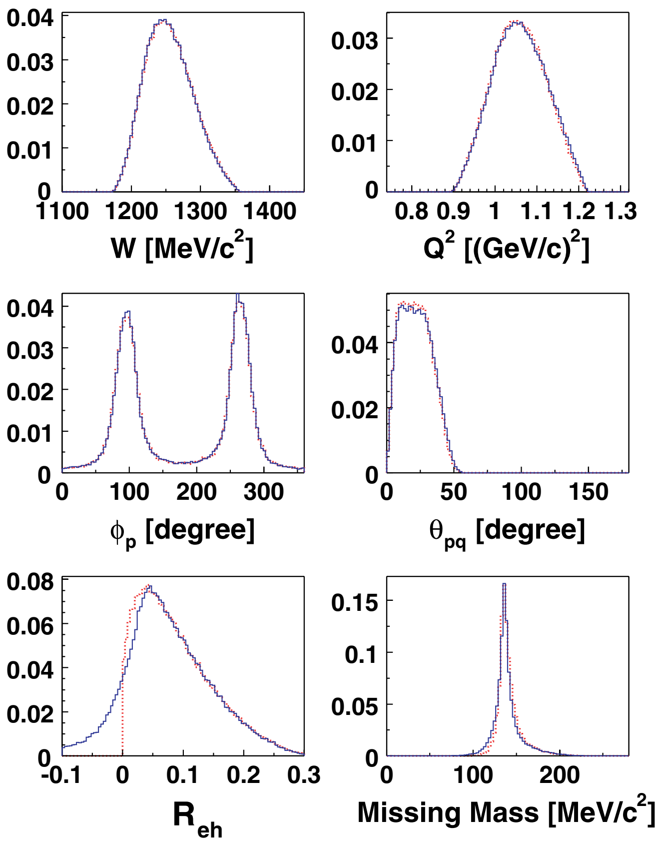

FIG. 3. (Color online) Comparison between observed (solid blue) and simulated (dotted red) distributions of kinematic variables for $\theta_{pq} = 0$ with $R_{eh} > 0.05$. The lower left panel shows the uncut distribution of R_{eh}.

C. Background

The acceptance cut $R_{eh} > 0.05$ suppresses the background from the elastic radiative tail quite strongly. The residual contribution is less than 0.4% at $\theta_{pq} = -90^\circ$ and much smaller at $\theta_{pq} = -50^\circ$. Hence, no corrections for this background were needed for the cross section or the unpolarized response functions. The background due to accidental coincidences was subtracted using time windows on both sides of the coincidence peak, applying the same particle identification and acceptance tests, and normalizing by width.

D. Cross section calculation

The virtual photoproduction cross section $\bar{\sigma}$ for a particular kinematic bin was determined by scaling the model cross section $\bar{\sigma}_{\text{model}}$ for that bin, evaluated for bin-centered kinematics, and applying various dead time and efficiency corrections according to

$$\bar{\sigma} = \frac{Y}{Y_{\text{MC}}} \bar{\sigma}_{\text{model}} \frac{f_{\text{CDT}} f_{\text{EDT}} f_{\text{abs}}}{\epsilon_{\text{trigger}} \epsilon_{\text{track}}}, \tag{10}$$

where Y and Y_{MC} are the observed and simulated yields, f_{CDT} corrects for computer dead ime, f_{EDT} corrects for electronics dead time, $\epsilon_{\text{trigger}}$ corrects for trigger efficiency, ϵ_{track} corrects for wire chamber and tracking efficiency, and f_{abs} corrects for proton absorption in materials between the scattering and detection. No correction was made for variation of luminosity with current because no systematic variation was observed in the luminosity monitor for the currents employed in the cross section measurements (20–60 μA).

The computer dead time was determined by comparing the coincidence scaler with the number of coincidence events recorded. In addition, the trigger supervisor has an internal dead time of approximately 100 ns, such that the electronics dead time for a 1 MHz rate in the trigger scintillators is about 10%. The electronics dead time was measured by sending pulser signals to one scintillator paddle in each arm and comparing the number of pulser signals recorded with the number counted by a scaler, correcting for computer dead time. The dependence of the electronic dead time upon strobe rate was then parametrized. The systematic uncertainty in the correction for electronic dead time was estimated to be about 1% at the highest rates [51].

The event reconstruction software rejects events with more than one track in either spectrometer. For the electron spectrometer, 10–12% of the events contained multiple tracks, while for the proton spectrometer, 1–12% contained multiple tracks depending upon the momentum and angle settings. We assume that the fraction of multiple-track events that contain a particle that would have satisfied the particle-identification criteria and other tests is the same as that for single-track events and apply corrections for each arm independently. In addition, we required valid tracks to contain three to eight hits in each VDC plane. The position dependence of tracking efficiency should be minimal for inelastic events which cover the spectrometer acceptances fairly uniformly. For the two settings with significant population by elastic scattering, the elastic scattering events were excluded from the calculation of tracking efficiency to minimize position-dependent effects upon trigger efficiency and to improve factorization of the tracking efficiencies for the two arms. The variation of the electron-arm tracking efficiency was used to obtain an estimated systematic uncertainty of 1.2% in that factor.

The triggers in each arm require coincidence between two scintillator planes and test the track direction. Thus, the trigger efficiency compares the total number of valid triggers with the total number of events with a least one hit in a scintillator. For the electron arm, we require events in both the numerator and the denominator to satisfy the Cerenkov test for electrons, and to contain only one track. For the proton arm, we also use one-track events but use the S0 scintillator instead of the Cerenkov detector. The net trigger efficiency of approximately 96.7%, with a systematic uncertainty of about 1%, is then the product of the efficiencies for the two arms.

Finally, we used a compilation of proton reaction cross sections to estimate the probability for proton absorption between scattering and detection. The net correction factor varied between 1.008 and 1.017 depending upon momentum.

E. Cross section results

We assume that the ratio between observed and simulated yields over the acceptance for a kinematic bin is very nearly

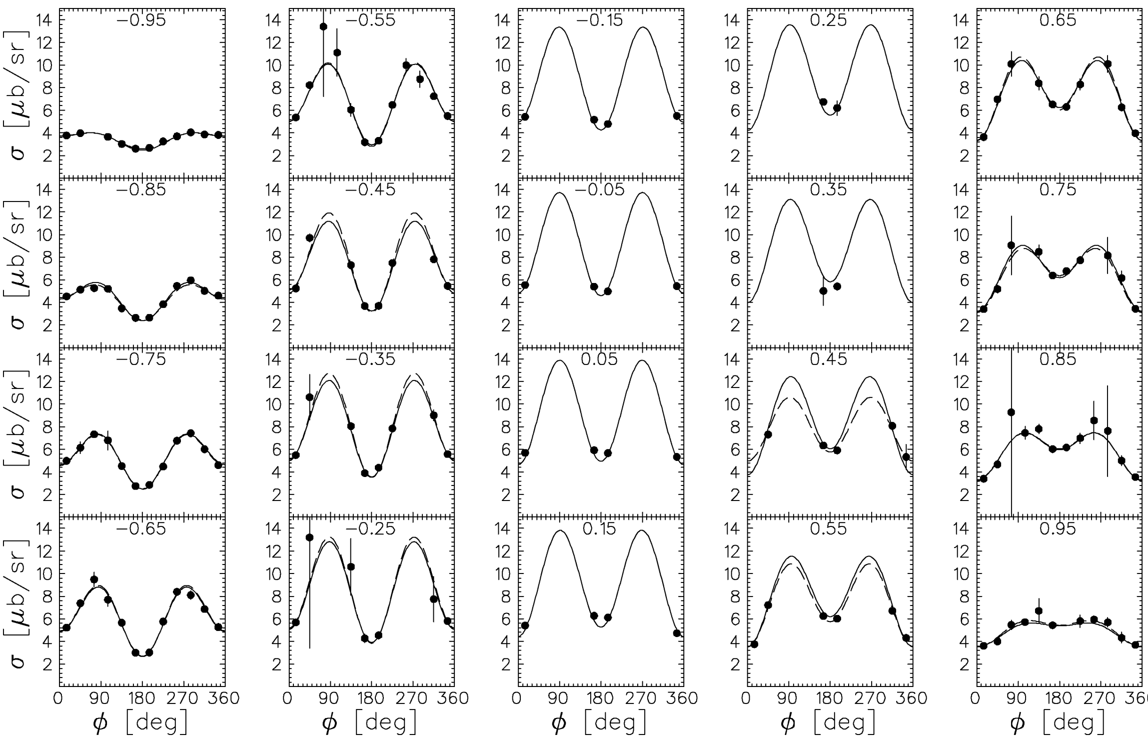

FIG. 4. Fits to the ϕ dependence of unpolarized cross section data with $(W, Q^2) = (1.23, 1.0)$. Each panel is labeled by the central x. Solid curves fit Legendre coefficients to the entire data set shown, while dashed curves fit response functions within each panel independently.

equal to the ratio between actual and model differential cross sections for the central kinematics of that bin. The accuracy of this assumption depends, of course, upon the bin size and the curvature of the differential cross section with respect to the binned variables. Events were accepted for $Q^2 = 1.0 \pm 0.2\,(\mathrm{GeV}/c)^2$. We used 10 bins in W between 1.17 and 1.35 GeV of width ± 0.01 GeV, 20 bins of x between -0.95 and $+0.95$ in steps of 0.1, and 12 bins of ϕ of 30° width. After dropping bins with negligible acceptance, approximately 1140 data were obtained for both differential cross section and beam analyzing power. These data are reported for central kinematics.

Figure 4 shows the ϕ dependence of the differential cross section for each x bin with $(W, Q^2) = (1.23, 1.0)$. The dashed curves fit R_{L+T}, R_{LT}, and R_{TT} for each (x, W, Q^2) independently to the ϕ dependence of Eq. (3a). Unfortunately, this procedure did not permit model-independent separation of R_{TT} from R_{L+T} for $x \approx 0$ because correlations were too large given the present ϕ acceptance. The solid curves fit Legendre coefficients to the (x, ϕ) dependence, thereby imposing a smooth x dependence that is not required by the extraction of unpolarized response functions. Nevertheless, both methods fit the data well and agree within the uncertainties estimated from covariances. Similar figures can be made for each (W, Q^2) bin, but are too numerous to display here.

The Legendre coefficients fit to the unpolarized cross section for $Q^2 = 1.0\,(\mathrm{GeV}/c)^2$ are compared in Figs. 5–7 with expansion coefficients for calculations based upon the MAID2003, DMT, SAID, and SL models obtained by inversion of Eq. (8). (More details about model calculations are given in Sec. VI A.) Although these calculations suggest that the sp truncation is probably adequate in the immediate vicinity of the Δ resonance, it appears that additional terms may be necessary elsewhere. Therefore, in addition to fits based upon sp truncation, we show fits with one additional free parameter for each response function within the the central W range, where the angular coverage and statistical precision are best. The models reproduce the even $L+T$ coefficients relatively well, although the W dependence of the SAID calculation for A_2^{L+T} is somewhat too flat. The models also reproduce the low-order coefficients for R_{LT} and R_{TT} relatively well. For R_{LT} the additional coefficient is determined relatively well near the middle of the W range and is consistent in both sign and magnitude with most model calculations. The resulting curvature in R_{LT} is small but definitely visible. Similarly, the data are consistent with the small negative linear coefficient predicted for R_{TT} but cannot determine higher-order coefficients. The additional term for R_{L+T} appears to be rather weak. The extra terms have very small effects upon the fitted value for lower coefficients of the same parity, but negligible effect upon those of opposite parity. Note that A_1^{L+T} is appreciably stronger than MAID, DMT, or SL predictions and exhibits an upturn for $W \gtrsim 1.3$ GeV that is absent from those models and that this result is not affected by the inclusion of terms beyond sp truncation.

Figures 5–7 also show similar results obtained by Joo *et al.* [18,52] at Jefferson Laboratory using CLAS. Here we show their results for the higher beam energy, 2.445 GeV, which has better statistical precision. However, the two experiments used different binnings with respect to Q^2. For the purposes of

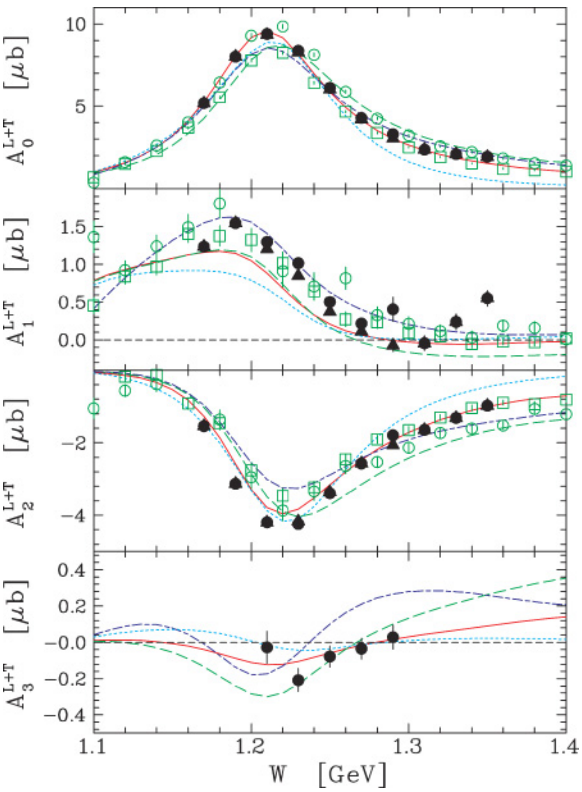

FIG. 5. (Color online) Legendre coefficients for R_{L+T} fit to differential cross sections at $Q^2 = 1.0\,(\mathrm{GeV}/c)^2$ compared with CLAS data. These quantities are defined in Eq. (8), where superscripts identify the response function and subscripts the degree of the Legendre polynomial. The filled triangles use the sp truncation, while in the central W range the filled circles include an extra term for each response function; the two sets of points often overlap. CLAS results scaled to $Q^2 = 1.0\,(\mathrm{GeV}/c)^2$ using a dipole form factor are shown as open green circles for $Q^2 = 0.9\,(\mathrm{GeV}/c)^2$ and open green squares for $Q^2 = 1.15\,(\mathrm{GeV}/c)^2$; only data for a beam energy of 2.445 GeV are shown. The CLAS analysis uses the same set of Legendre coefficients as the filled triangles. These results are compared with MAID2003 (red solid), DMT (green dashed), SAID (blue dash-dotted), and SL (cyan dotted) calculations.

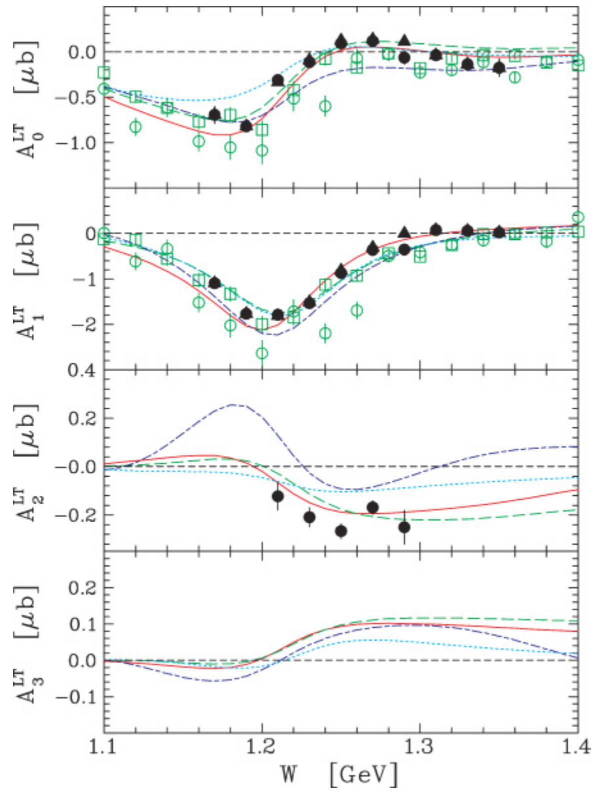

FIG. 6. (Color online) Same as Fig. 5, but for R_{LT}.

this comparison, we assume that the Legendre coefficients are proportional to the square of a dipole form factor and rescale the CLAS data for $Q^2 = 0.9$ and $1.15\,(\mathrm{GeV}/c)^2$ to a common value of $1.0\,(\mathrm{GeV}/c)^2$. Note, however, that for a given W, ϵ is higher for $Q^2 = 0.9$ than for $1.15\,(\mathrm{GeV}/c)^2$ and that ϵ for our experiment is higher than for either of the CLAS data sets. We observe good qualitative agreement between these data sets, but there are significant differences in detail. For example, our A_2^{L+T} is systematically stronger for low W than in CLAS data. Nor does the form-factor scaling prescription bring the two CLAS data sets for LT coefficients in agreement with each other, but the higher Q^2 data also appear to show more scatter. On the other hand, the curvature we see in the x dependence of R_{LT} clearly requires at least one term beyond sp truncation; this is shown in more detail in Sec. VI B. Perhaps the omission of A_2^{LT} from the CLAS analysis is partly responsible for discrepancies in the lower coefficients.

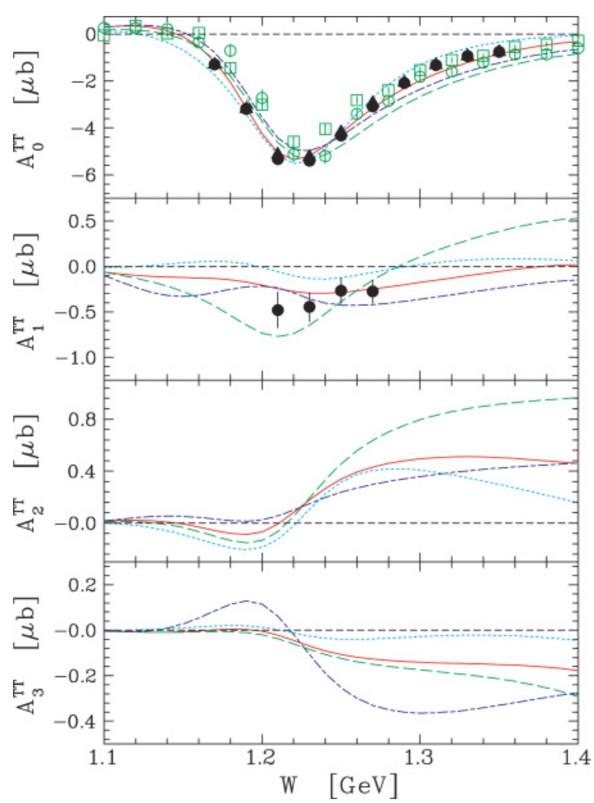

FIG. 7. (Color online) Same as Fig. 5, but for R_{TT}.

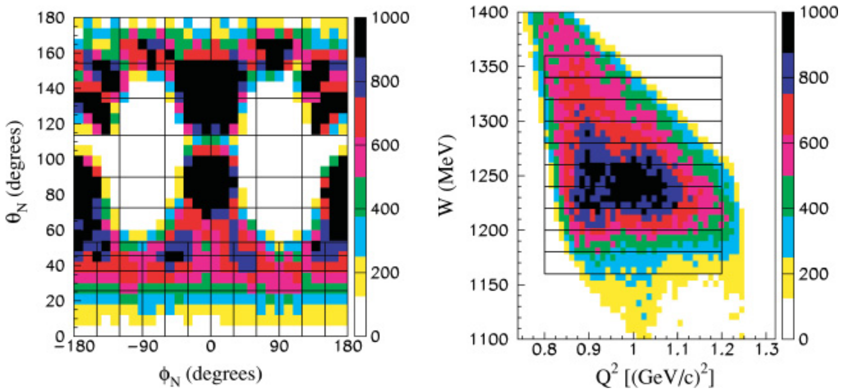

FIG. 8. (Color online) Kinematic acceptance and binning for the polarization analysis. Left: angular acceptance for (ϕ_N, θ_N) in the c.m. frame. Right: (Q^2, W) acceptance. These composite figures include several runs from all spectrometer settings, where the number of runs for each setting was chosen to display similar statistics in every region. The left side includes events in the outer box of the right side, namely, $1.16 \leqslant W \leqslant 1.36$ GeV and $0.8 \leqslant Q^2 \leqslant 1.2\,(\mathrm{GeV}/c)^2$.

V. POLARIZATION ANALYSIS

The kinematic acceptances and binning for the polarization analysis are illustrated in Fig. 8. Kinematic focusing of the reaction into a laboratory cone with an opening angle of about 13° and relatively large spectrometer apertures provide considerable out-of-plane coverage and access to most of the response functions. In fact, the azimuthal acceptance for nucleons forward of 50° or backward of 150° in the c.m. is practically complete. The angular bins were chosen to distribute counts fairly uniformly among the populated bins. The right side shows that the best kinematic coverage and statistics were obtained for $1.21 \leqslant W \leqslant 1.29$ GeV, but there is useful acceptance over a broader range.

A. Polarization analysis using likelihood method

Let $\vec{T} = (T_t, T_n, T_\ell) = \vec{P} + hP_e\vec{P}'$ represent the proton recoil polarization at the target in the πN center-of-mass system, where h denotes the sign of the electron helicity and P_e is the magnitude of the beam polarization, and let $\vec{F} = (F_x, F_y, F_z)$ represent the polarization at the focal-plane polarimeter with $\hat{z}$ along the nucleon momentum and $\hat{y}$ leftward with respect to the vertical plane containing the nucleon momentum. These vectors are related by a spin transport matrix S, representing a sequence of transformations from the target c.m. frame to the local FPP coordinate system, such that $F = ST$. The spin transport matrix is evaluated for each event.

The polarization components at the target were extracted from the azimuthal distribution for scattering by the FPP analyzer using the method of maximum likelihood [53]. The likelihood function takes the form

$$L = \prod_{\text{events}} \frac{1}{2\pi}\left(1 + \xi - \varepsilon_x \sin\phi_{\text{fpp}} + \varepsilon_y \cos\phi_{\text{fpp}}\right) \tag{11}$$

of a product of the scattering probabilities for each event that satisfies the selection criteria for a given kinematic bin. The azimuthal scattering angle ϕ_{fpp} is measured counterclockwise from the final $\hat{x}$ axis for each event, and ξ represents the false (instrumental) asymmetry, discussed in Sec. V E. The ϵ coefficients are given by

$$\varepsilon_\alpha = A_y(\theta_{\text{fpp}}) \sum_\beta S_{\alpha\beta} T_\beta, \tag{12}$$

where $A_y(\theta_{\text{fpp}})$ is the analyzing power for polar scattering angle θ_{fpp}, $\alpha \in \{x, y, z\}$ identifies the polarization components at the FPP, $\beta \in \{t, n, \ell\}$ identifies components of $\vec{T}$ at the target in the πN c.m. frame, and $S_{\alpha\beta}$ are elements of the spin-transport matrix. Although the scattering probability for each event is independent of the longitudinal polarization, the variation of spin transport within the experimental acceptance offers access to all three components of polarization at the target.

If the asymmetries $(\varepsilon_x, \varepsilon_y, \xi)$ are small, the problem reduces to the linear system

$$V = \Lambda \cdot R, \tag{13}$$

where

$$R = (P_t, P_n, P_\ell, P_t', P_n', P_\ell') \tag{14}$$

is the result vector,

$$V_\alpha = \sum_i \frac{\lambda_{i\alpha}}{1 + \xi_i} \tag{15}$$

is an element of the measurement vector, and

$$\Lambda_{\alpha,\beta} = \sum_i \frac{\lambda_{i\alpha}}{1 + \xi_i}\frac{\lambda_{i\beta}}{1 + \xi_i} \tag{16}$$

is an element of the design matrix where the Greek indices $\{\alpha, \beta = 1, 6\}$ correspond to elements of the result vector and the Latin index i enumerates events that satisfy the selection criteria for a particular kinematic bin. Elements of the result vector represent acceptance-averaged components of recoil polarization that are taken to be constant within each kinematic bin. Conversely, the elements of the measurement vector and design matrix accumulate contributions

$$\begin{aligned}
\xi &= a_0 \sin\phi_{\text{fpp}} + b_0 \cos\phi_{\text{fpp}} + c_0 \sin 2\phi_{\text{fpp}} + d_0 \cos 2\phi_{\text{fpp}},\\
\lambda_1 &= A(\theta_{\text{fpp}})(S_{yt}\cos\phi_{\text{fpp}} - S_{xt}\sin\phi_{\text{fpp}}),\\
\lambda_2 &= A(\theta_{\text{fpp}})(S_{yn}\cos\phi_{\text{fpp}} - S_{xn}\sin\phi_{\text{fpp}}),\\
\lambda_3 &= A(\theta_{\text{fpp}})(S_{y\ell}\cos\phi_{\text{fpp}} - S_{x\ell}\sin\phi_{\text{fpp}}),\\
\lambda_4 &= hP_e\lambda_1,\\
\lambda_5 &= hP_e\lambda_2,\\
\lambda_6 &= hP_e\lambda_3,
\end{aligned}$$

which are evaluated independently for each event, where the event indices have been suppressed.

B. Extraction of polarized response functions using likelihood method

Binning with respect to ϕ can be avoided by using Eq. (3a) to express the likelihood function

$$L = \prod_{\text{events}} \frac{1}{2\pi}(1 + \xi + \eta \cdot R) \tag{17}$$

in terms of response functions

$$R = \left(R^{t}_{LT}, R^{t}_{TT}, R^{n}_{L+T}, R^{n}_{LT}, R^{n}_{TT}, R^{\ell}_{LT}, R^{\ell}_{TT}, R'^{t}_{LT}, R'^{t}_{TT}, R'^{n}_{LT}, R'^{\ell}_{LT}, R'^{\ell}_{TT}\right) \tag{18}$$

with coefficients

$$\begin{aligned}
\bar{\sigma}\eta_1 &= \lambda_1 \nu_0 \nu_{LT} \sin\phi,\\
\bar{\sigma}\eta_2 &= \lambda_1 \nu_0 \nu_{TT} \sin\theta \sin 2\phi,\\
\bar{\sigma}\eta_3 &= \lambda_2 \nu_0 \nu_{T} \sin\theta,\\
\bar{\sigma}\eta_4 &= \lambda_2 \nu_0 \nu_{LT} \cos\phi,\\
\bar{\sigma}\eta_5 &= \lambda_2 \nu_0 \nu_{TT} \sin\theta \cos 2\phi,\\
\bar{\sigma}\eta_6 &= \lambda_3 \nu_0 \nu_{LT} \sin\theta \sin\phi,\\
\bar{\sigma}\eta_7 &= \lambda_3 \nu_0 \nu_{TT} \sin^2\theta \sin 2\phi,\\
\bar{\sigma}\eta_8 &= \lambda_4 \nu_0 \nu'_{LT} \cos\phi,\\
\bar{\sigma}\eta_9 &= \lambda_4 \nu_0 \nu'_{TT} \sin\theta,\\
\bar{\sigma}\eta_{10} &= \lambda_5 \nu_0 \nu'_{LT} \sin\phi,\\
\bar{\sigma}\eta_{11} &= \lambda_6 \nu_0 \nu'_{LT} \sin\theta \cos\phi,\\
\bar{\sigma}\eta_{12} &= \lambda_6 \nu_0 \nu'_{TT},
\end{aligned}$$

which incorporate the azimuthal dependencies event by event. This method also permits the leading polar angle dependencies to be incorporated explicitly event-by-event, such that the extracted quantities are response functions binned with respect to $x = \cos\theta$.

The coefficients for response functions depend upon the unpolarized differential cross section for each event, which varies within the kinematical bin. This cross section was obtained by scaling the model cross section (MAID2000) calculated at the event kinematics by the ratio between the *sp* Legendre fit to the experimental cross section and the model cross section for the central kinematics of the bin. This Legendre fit is discussed in Sec. IV E. The Legendre parametrization can sometimes produce nonpositive cross sections for some events with kinematics at the edges of the acceptance; for those events, we simply use the MAID2000 cross section and recognize that these extreme kinematics contribute very little to acceptance-averaged quantities anyway.

C. Track reconstruction and selection

The chambers were aligned with respect to each other, and the VDCs using *straight-through* events obtained by removing the carbon analyzer. The track reconstruction algorithms are described in Ref. [38]. For our purposes, it is sufficient to note that the hit multiplicity within the straw chambers is sufficient to define tracks before and after the carbon analyzer. Thus, we can impose a requirement that the scattering vertex lie within the carbon plates used for a particular measurement. We also require that the polar scattering angle be in the range $5^\circ \leqslant \theta_{\text{fpp}} \leqslant 20^\circ$, where the lower limit enhances the analyzing power by suppressing unpolarized Coulomb scattering and the upper limit keeps instrumental asymmetries small. Finally, to minimize false asymmetries due to the finite size of the rear chambers, we impose a *cone test* that demands that the entire cone subtended by the polar scattering angle for each track intercepts both rear chambers. The rear chambers are actually large enough that only a few percent of the events in the accepted θ_{fpp} range fail the cone test.

D. Calibration

We fitted an extension of the McNaughton parametrization [54] of the $p+^{12}$C analyzing power using earlier Hall A data supplemented by new measurements of elastic scattering by the proton for momenta of 0.818, 1.066, 1.188, and 1.378 GeV/c in order to provide analyzing power data closer to some of the present kinematic settings. Our measurements of G_{Ep}/G_{Mp} at $Q^2 = 1.0$ and $1.4\,(\text{GeV}/c)^2$ are in good agreement with those of Ref. [55].

E. False asymmetry

The one-photon exchange approximation predicts that the helicity-independent recoil polarization for elastic electron-proton scattering vanishes. Assuming that the two-photon contribution is negligible, we used this reaction to measure the false instrumental asymmetries arising from misalignment, detector or tracking inefficiencies, variations of path lengths in the analyzer, and other mechanisms. We express the detection probability in the form

$$\begin{aligned}
f_h(\theta_{\text{fpp}}, \phi_{\text{fpp}}) = f_0(\theta_{\text{fpp}}, \phi_{\text{fpp}}) \frac{1}{2\pi}(1 &- h\varepsilon_x \sin\phi_{\text{fpp}}\\
&+ h\varepsilon_y \cos\phi_{\text{fpp}} + a_0 \sin\phi_{\text{fpp}} + b_0 \cos\phi_{\text{fpp}}\\
&+ c_0 \sin 2\phi_{\text{fpp}} + d_0 \cos 2\phi_{\text{fpp}}),
\end{aligned} \tag{19}$$

where the coefficients (a_0, b_0, c_0, d_0) parametrize the false asymmetry, while the coefficients $(\varepsilon_x, \varepsilon_y)$ depend upon the helicity-dependent recoil polarization and the FPP analyzing power. Thus, the false asymmetry coefficients are obtained by Fourier analysis of

$$\begin{aligned}
\frac{f_+ + f_-}{2f_0} = \frac{1}{2\pi}(1+\xi) = \frac{1}{2\pi}(1 &+ a_0 \sin\phi_{\text{fpp}} + b_0 \cos\phi_{\text{fpp}}\\
&+ c_0 \sin 2\phi_{\text{fpp}} + d_0 \cos 2\phi_{\text{fpp}}).
\end{aligned} \tag{20}$$

Data for elastic scattering were taken at five proton momenta between 0.785 and 0.851 GeV/c and at 1.066 and 1.188 GeV/c. The dependence of false asymmetries upon δ are shown in Fig. 9 for $5^\circ < \theta_{\text{fpp}} < 20^\circ$. Only the coefficient of $\cos\phi_{\text{fpp}}$ shows a significant dependence upon δ that can be attributed, in part, to its correlation with the average path length of scattered particles in the carbon analyzer. This dependence was parametrized by a linear function. The other three coefficients are essentially independent of δ with average values less than 1%. No significant dependence upon proton central momentum is apparent over this range.

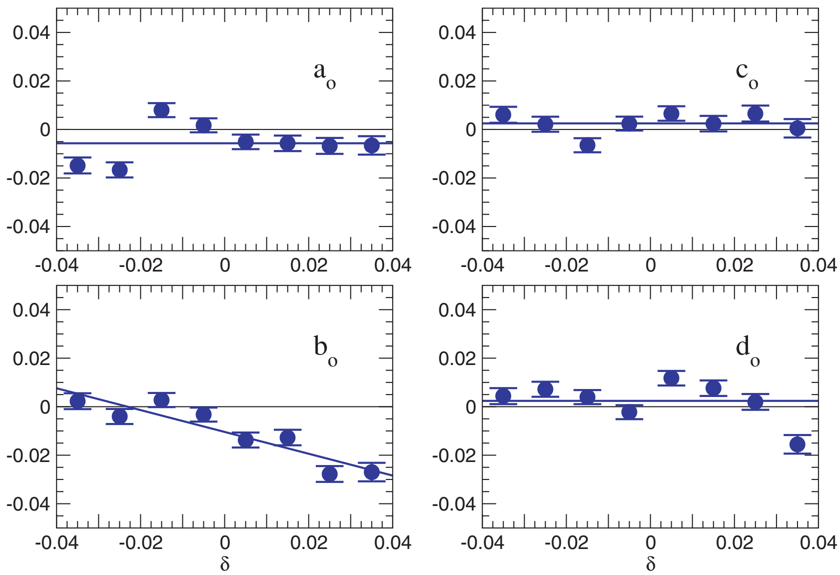

FIG. 9. (Color online) Dependence of measured Fourier coefficients for false asymmetry upon spectrometer relative momentum are shown with average values (a_0, c_0, d_0) or a linear fit (b_0) as blue lines.

F. Background subtraction

The polarization response functions were corrected for two types of background: the elastic radiative tail and accidental coincidences. Corrections for the unresolved contribution of the elastic radiative tail were made using the likelihood function because those contributions varied strongly with both θ and ϕ. Thus, we generalize Eq. (12) to

$$\varepsilon_\alpha = A_y(\theta_{\rm fpp}) \sum_\beta \left(f_1 S^{(1)}_{\alpha\beta} T^{(1)}_\beta + f_2 S^{(2)}_{\alpha\beta} T^{(2)}_\beta \right), \tag{21}$$

where $f_1 + f_2 = 1$, and where $T^{(1)}$ is the polarization for Δ excitation and $T^{(2)}$ is the polarization for elastic scattering. Note that the spin transformation matrix $S^{(2)}$ for elastic scattering differs from $S^{(1)}$ for pion production because the polarization vectors for the two reactions are normally evaluated in different frames. Thus, $S^{(2)}$ omits the Wigner rotation and assumes that the proton emerges parallel to $\vec{q}$. The relative weights depend upon the (W, Q^2, x, ϕ) bin and were obtained by fitting the missing-mass distributions for each bin with appreciable elastic contamination. This contribution is actually very small and is only visible for the $\theta_{\rm c.m.} = -90^\circ$ setting. Generalization of the likelihood formula, Eq. (17), is straightforward. The elastic polarizations were computed from the parametrizations of G_{Ep} and G_{Mp} found in Refs. [56,57], but the results are insensitive to the small differences between models.

Accidental background was subtracted by analyzing both in-time and out-time events in the same manner. For polarization we obtain

$$P = \frac{P_p - r P_b}{1 - r}, \tag{22a}$$

$$(\delta P)^2 = \frac{(\delta P_p)^2 + (r\delta P_b)^2}{(1-r)^2}, \tag{22b}$$

where $P_p \pm \delta P_p$ is the measurement for the in-time region, $P_b \pm \delta P_b$ is the result for the out-time region, and r is the ratio between the widths of these regions. Similarly, for response functions we obtain

$$R = R_p - r R_b, \tag{23a}$$

$$(\delta R)^2 = (\delta R_p)^2 + (r \delta R_b)^2, \tag{23b}$$

where $R_p \pm \delta R_p$ and $R_b \pm \delta R_b$ are obtained for in-time and out-time regions, respectively. The effect of background subtraction is generally difficult to discern in standard figures and is always much less than the statistical uncertainty in these measurements.

G. Pseudodata tests

The analysis procedures were tested using pseudodata. For each accepted event, response functions and polarizations at the target were computed based upon the MAID2000 model. The observed polar scattering angle $\theta_{\rm fpp}$ was retained but the azimuthal scattering angle $\phi_{\rm fpp}$ was sampled randomly. This value of $\phi_{\rm fpp}$ was retained if the likelihood L calculated according to Eq. (11) was greater than the next random number thrown and rejected otherwise. This procedure was iterated until a value of $\phi_{\rm fpp}$ was selected. Contributions to V and Λ were then accumulated, and the pseudodata were analyzed in the same manner as real data.

These tests demonstrate that model input for response functions is recovered within statistical uncertainties, but that there are sometimes inconsistencies in the ϕ dependence of polarization data. This problem arises because relatively large bins in ϕ are needed to obtain useful statistical precision, but some of the spin-transport matrix elements can exhibit broad distributions with respect to other variables in part due to kinematic focusing in the laboratory frame. Under those conditions, the acceptance-averaged polarization can differ appreciably from model values for the central kinematics of a bin. These difficulties are much smaller for response functions because binning with respect to ϕ is not necessary; all ϕ values contribute to the determination of a response function and their coefficients are evaluated properly for each event. Explicit eventwise weighting with the leading factors of $\sin\theta$ also reduces the effects of acceptance averaging on the response functions as defined in Eq. (3). Therefore, we focus upon the response-function data and do not consider polarization binned with respect to ϕ further. A more detailed report on the pseudodata analysis is provided in Ref. [58].

H. Acceptance averaging

Multipole amplitudes and Legendre coefficients are functions of (W, Q^2), but the acceptance averaged $(\overline{W}, \overline{Q^2})$ depend upon x. Consequently, extraction of these quantities from angular distributions can be distorted by the x variations of $(\overline{W}, \overline{Q^2})$. Such distortions can artificially enhance terms for large ℓ_π. Two methods for compensating for such distortions have been tested using both pseudodata and real data. The additive method is based upon the first-order expansion

$$R(W, Q^2, \bar{x}, \bar{\epsilon}) = R(\overline{W}, \overline{Q^2}, \bar{x}, \bar{\epsilon}) - \frac{\partial R}{\partial W}(\overline{W} - W) - \frac{\partial R}{\partial Q^2}(\overline{Q^2} - Q^2), \qquad (24)$$

where overlines indicate acceptance averaging and the derivatives are evaluated at central kinematics using a model such as MAID. For this experiment, $\overline{Q^2} - Q^2$ tends to be much more important than $\overline{W} - W$. Additive kinematic corrections have the advantage that variations of both W and Q^2 can be accommodated, but this procedure has the disadvantage that it relies upon a model and we have no model that provides a uniformly good fit to all of the response functions. While that is not a problem for pseudodata, the use of an inaccurate model to make kinematic corrections to real data could introduce more serious errors than it corrects. Therefore, a second procedure based upon form factors was tested. Assuming that all response functions share a common form factor, and that kinematic corrections are dominated by the x dependence of $\overline{Q^2}$, we postulate

$$R(W, Q^2, \bar{x}) = R(\overline{W}, \overline{Q^2}, \bar{x})(G(Q^2)/G(\overline{Q^2}))^2 \qquad (25)$$

and approximate $G(Q^2)$ by the usual dipole form factor $G_D(Q^2) = (1 + Q^2/\Lambda^2)^{-2}$ where $\Lambda^2 = 0.71\,(\mathrm{GeV}/c)^2$. This multiplicative procedure does not compensate for variations of $\overline{W}$, but for this experiment these variations are much smaller than those for $\overline{Q^2}$.

Figure 10 compares pseudodata with multiplicative kinematic corrections with the model for central kinematics. The open squares show raw response functions extracted from pseudodata, while open red circles show acceptance-averaged response functions from MAID2000. The agreement between these data sets, modulo statistical fluctuations, demonstrates the internal consistency of the simulation/analysis program. However, the x dependence of $\overline{Q^2}$ can produce significant systematic deviations from the input model (solid curves) evaluated at central kinematics, especially for R'^{n}_{TT}. Recognizing that $\overline{Q^2} \approx 0.94$ for $x > 0.5$ or $1.06\,(\mathrm{GeV}/c)^2$ for $x < -0.5$, we observe that the pseudodata for R'^{n}_{TT} do cluster around the model curve for the appropriate Q^2. Even the abrupt transition across $x = 0$ is reproduced. The solid circles show that "centered" pseudodata adjusted according to Eq. (25) cluster better around the model curves for central kinematics. Therefore, distortion of multipole amplitudes by the x dependence of

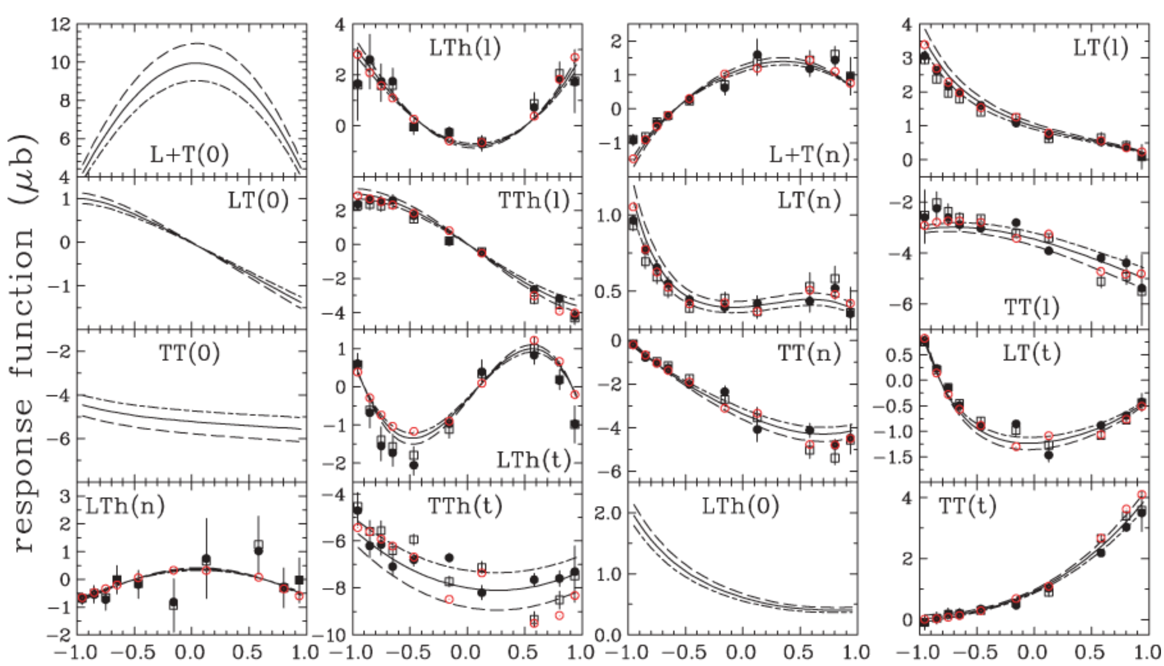

FIG. 10. (Color online) Pseudodata data for response functions at $W = 1.23 \pm 0.01$ GeV and $Q^2 = 1.0 \pm 0.2\,(\mathrm{GeV}/c)^2$ are compared with the input model (MAID2000) at the central kinematics (solid curves) and with neighboring values of Q^2 representative of the x dependence of acceptance averaging; dashed curves show $Q^2 = 0.94$ and dashed-dotted curves show $Q^2 = 1.06\,(\mathrm{GeV}/c)^2$. Acceptance-averaged calculations are shown as red open circles and pseudodata as open squares. Filled circles show pseudodata with multiplicative kinematic corrections based upon the dipole form factor.

$\overline{Q^2}$ should be minimized by fitting centered data. We find that the multiplicative corrections move the pseudodata in the directions indicated by ratios between acceptance-averaged calculations and those for central kinematics. The net effect is to reduce the scatter in the pseudodata and to remove many systematic deviations attributable to the x dependence of $\overline{Q^2}$. On the other hand, we have the qualitative impression that the corrections are sometimes a little too large, although no attempt has been made to quantify that impression. One could reduce the size of the multiplicative correction by increasing the dipole mass Λ, but the $N \to \Delta$ form factor is actually steeper (smaller Λ) than the standard dipole form factor. Furthermore, changes to the correction by replacing the dipole with a parametrization of the $N \to \Delta$ form factor are quite small.

Therefore, we adopted the multiplicative correction based upon the dipole form factor as the standard method for bin centering. The figures in the remainder of this paper show recoil polarization response functions plotted at $\overline{x}$ with bin-centering corrections for $\overline{Q^2}$. Legendre and multipole fits were made to the data in this form.

I. Systematic uncertainties

1. Response functions

There are several types of normalization uncertainty that affect the response-function data. These include uncertainties in the unpolarized differential cross section used to normalize the likelihood, the FPP analyzing power, and for helicity-dependent responses, the beam polarization. Although these systematic uncertainties do vary to some degree with spectrometer settings, beam conditions, and time, those variations are small compared with the statistical uncertainties. Therefore, we believe it is sufficient to estimate average systematic uncertainties for those quantities without tracking the propagation of particular settings through event sorting. The typical systematic uncertainties in the differential cross section data are about $\pm 3\%$ point-to-point, so we assume that the uncertainty in the parametrized cross section used in the likelihood analysis is also about $\pm 3\%$. Similarly, the systematic relative uncertainty for Compton measurements of beam polarization is estimated to be about 1.4% [40]. Finally, the relative uncertainties in average analyzing power reported by Punjabi *et al.* [37] are in the 1–2% range. Because we do not consider thickness or momentum variations, we adopt a fairly conservative estimate of $\delta A_y/A_y = 0.02$. Therefore, the normalization uncertainties are approximately $\pm 3.6\%$ for helicity-independent or $\pm 3.9\%$ for helicity-dependent response functions.

The evaluation of other types of systematic error requires replaying the data subject to a perturbation of one of the analysis parameters. Thus, the uncertainty due to subtraction of the elastic background was obtained by comparing replays with and without that subtraction. Because the contamination fractions binned in ϕ were difficult to determine, we assumed their relative uncertainties to be 100% and estimated the corresponding uncertainties in response functions as

$$\delta R_\alpha = \left| R_\alpha^{(2)} - R_\alpha^{(1)} \right|, \tag{26}$$

where $R_\alpha^{(1)}$ and $R_\alpha^{(2)}$ represent response function α with and without elastic subtraction. Similarly, the uncertainty in corrections for false asymmetry were estimated as

$$\delta R_\alpha = 0.1 \left| R_\alpha^{(2)} - R_\alpha^{(1)} \right|, \tag{27}$$

where the relative uncertainty in false asymmetry was estimated to be $\pm 10\%$ and is multiplied by the difference in response functions obtained with and without false asymmetry in the likelihood function.

A similar procedure was also applied for the spin transport matrix. The sensitivity of response functions to uncertainties in the spin rotation matrix is illustrated in Fig. 11 for

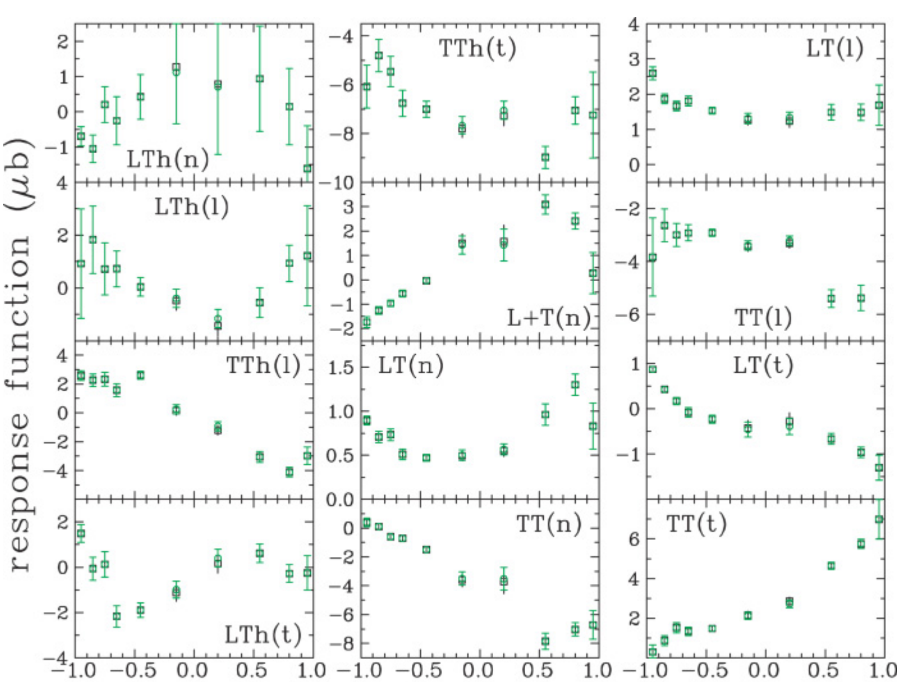

FIG. 11. (Color online) Sensitivity of response functions for $W = 1.23$ GeV to uncertainties in the spin rotation matrix. Open black squares were obtained using the COSY model, while open green circles are based upon the Pentchev model; the two sets overlap almost completely. For the Pentchev analysis, inner error bars are statistical while outer error bars include systematic errors due to uncertainties in precession angles and optical matrix elements; however, the systematic errors are generally too small to see.

$W = 1.23$ GeV. The black squares were obtained using the COSY model, while the green circles were obtained using a simpler geometrical model by Pentchev in terms of six parameters consisting of two trajectory angles and four matrix elements coupling spin components [37,59]. The almost complete overlap between these data sets demonstrates that this geometrical model accurately reproduces the COSY model. Therefore, we can estimate systematic errors in response functions due to uncertainties in spin rotation by comparing results obtained from independent perturbations of each of the six parameters of the geometrical model by its estimated uncertainty and combining in quadrature differences with respect to nominal parameters. We use the same systematic uncertainties for those parameters as in Refs. [37,59]. The green error bars in Fig. 11 include an inner statistical portion shown with end caps and a total error without end caps. However, rarely can one discern the systematic contribution to the total bar, because the composite contribution of spin rotation errors is almost always small relative to statistical uncertainties.

The net systematic uncertainties in response functions, consisting of the quadrature sum of all contributions discussed in this section, tend to be dominated by the normalizations and are almost always small compared with statistical uncertainties. Many of the figures show statistical uncertainties as inner error bars with end caps and total uncertainties as outer error bars without end caps. The systematic contributions are occasionally visible for Legendre coefficients or multipole amplitudes but are rarely visible for response functions.

2. *Legendre coefficients and multipole amplitudes*

Let y represent a fitted quantity, such as a quadrupole ratio, Legendre coefficient, or multipole amplitude, and let β represent a calibration parameter or a scale factor applied to one of the corrections, such as false asymmetry. We estimate the systematic uncertainty $(\delta y)_{\rm sys}$ by adding in quadrature numerical derivatives, i.e.,

$$(\delta y)^2_{\rm sys} = \sum_i \left(\frac{\partial y}{\partial \beta_i}\delta\beta_i\right)^2 = \sum_i (y(\beta_i + \delta\beta_i) - y(\beta_i))^2, \quad (28)$$

estimated by performing a series of fits in which each calibration parameter is perturbed in turn. Therefore, Legendre and multipole fits to such data sets begin with the results of the best fit for nominal calibration parameters and usually require only a few iterations to determine small displacements of the minimum on the χ^2 hypersurface. We assume that the desired local minimum is related to the best fit by a small distortion of the χ^2 hypersurface produced by small changes in the data set due to perturbation of an analysis parameter. By starting with the nominal best fit, we minimize the chance that the fitting procedure might find a different local minimum. With enough care in the fitting procedure, we find that changes in fitted Legendre coefficients or multipole amplitudes due to variation of spin-rotation parameters or omission of false asymmetry or elastic subtraction are typically small.

In addition to systematic uncertainties considered in the previous section, Legendre and multipole analyses also include an estimate of the uncertainty due to the kinematic or bin-centering correction. The customary dipole form factor should describe the Q^2 dependence of nonresonant contributions fairly well, but the $N \to \Delta$ form factor is known to have a more rapid Q^2 dependence. The best description is probably intermediate between these models. We estimated the uncertainty in fitted Legendre coefficients and multipole amplitudes due to the choice of bin-centering form factor by comparing fits for the dipole and $N \to \Delta$ form factors, assigning a systematic uncertainty equal to the difference between the two fits. The dipole form factor is given by $G_D(Q^2) = (1 + Q^2/\Lambda^2)^{-2}$ where $\Lambda^2 = 0.71\,({\rm GeV}/c)^2$. For the $N \to \Delta$ form factor, we use the Sato-Lee parametrization $G_{N\Delta} = (1 + aQ^2)\exp(-bQ^2)G_D$ with $a = 0.154$ and $b = 0.166\,({\rm GeV}/c)^{-2}$ [60]. However, the difference between these form factors over the range of $\overline{Q^2} - Q^2$ for this experiment is too small to produce a visible difference in the projected data or fitted angular distributions.

The systematic uncertainties in fitted Legendre coefficients and multipole amplitudes contain a total of 12 contributions added in quadrature, each requiring a fit to the relevant data set. Variations of the cross section, FPP analyzing power, beam polarization, bin centering, false asymmetry, and elastic subtraction are all compared with the best fit for data obtained using COSY spin rotation. The six contributions to the spin rotation uncertainty are estimated using differences with respect to data based upon the nominal Pentchev model. The net systematic errors in these quantities are generally small compared with statistical uncertainties. Figures showing fitted quantities with statistical and total errors bars can be found in the separate reports on Legendre coefficients [61] and multipole amplitudes [62].

J. Summary of experimental data

Near the middle of our (W, Q^2) acceptance, we obtained complete angular distributions for 16 response functions, 14 separated plus 2 Rosenbluth combinations for $\varepsilon \sim 0.95$. The angular coverage and statistical precision are clearly best in the central W range, $1.21 \leqslant W \leqslant 1.29$ GeV. Data tables are on deposit with EPAPS [83]. These tables give both raw and bin-centered data with both nominal and acceptance-averaged kinematics. Tables of Legendre coefficients and multipole amplitudes are also included.

VI. RESULTS

A. Comparison with models

In this section, we compare our data for response functions with calculations using four recent models. We provide very brief summaries of the models and refer to original sources for more detailed information. A recent review of these and related models has also been provided by Burkert and Lee [63].

The SAID model [13,64] parametrizes a photoexcitation multipole amplitude A in the form

$$A = (A_B + A_Q)(1 + it_{\pi N}) + A_R t_{\pi N} + (C + iD)\left({\rm Im}t_{\pi N} - t^2_{\pi N}\right), \quad (29)$$

where $t_{\pi N}$ is a t-matrix fit to πN elastic scattering data that enforces the Fermi-Watson theorem [65] below the two-pion threshold, A_R is parametrized as a polynomial in E_π with the correct threshold behavior for each partial wave, A_B is a partial wave of the pseudoscalar Born amplitude, and A_Q is parametrized using Legendre functions of the second kind. Recent extensions also include energy-dependent polynomials C and D. Electroexcitation amplitudes also include form factors in Q^2. We are now using the WI03 version of SAID [66].

The Mainz unitary isobar model [67], known as MAID, parametrizes resonant contributions to multipole amplitudes using the Breit-Wigner form

$$A = \bar{A}(Q^2)C_{\pi N} f_{\gamma N}(W) \frac{\Gamma_{\text{tot}} W_R e^{i\psi}}{W_R^2 - W^2 - iW_R\Gamma_{\text{tot}}} f_{\pi N}(W), \tag{30}$$

where W_R is the resonance mass, Γ_{tot} is its total width at resonance, $C_{\pi N}$ is an isospin factor, and $\bar{A}$ is a form factor. The W dependence of the electroexcitation vertex and its pseudothreshold behavior is represented by $f_{\gamma N}$, while $f_{\pi N}$ describes the $R \to \pi N$ decay in terms of an energy-dependent partial width, $\Gamma_{\pi N}(W)$, and appropriate phase-space and penetrability factors. Nonresonant amplitudes are computed using Born and vector-meson diagrams with a mixed πNN coupling that interpolates between pseudovector coupling at low c.m. momentum p_π and pseudoscalar coupling at high p_π. Background amplitudes are unitarized with the $(1 + it_{\pi N})$ factor, as above, while resonant contributions are unitarized by adjusting the phase ψ such that the total phase of the resonant contribution is given by the SAID partial-wave analysis for πN elastic scattering. Thus, ψ depends upon both W and Q^2 and varies with multipole. The event generator used for data analysis employed MAID2000, but here we will show calculations using the updated MAID2003 version [68,69].

Both MAID2003 and SAID WI03 were optimized with respect to similar data sets and consider a very broad range of kinematics for the $p\pi^0$ channel. Both use the same πN phase shift analysis [13]. In the present kinematic region, the older differential cross sections are primarily from Refs. [70,71]. Newer differential cross sections from Jefferson Laboratory include angular distributions from Hall B [18] and data for $x < -0.825$ from Hall A [20]. Neither analysis included any polarization data for π^0 electroproduction. However, neither group has published a detailed comparison between these data and their fits.

The Dubna-Mainz-Taipei (DMT) model [72,73] is based upon MAID but employs a more sophisticated analysis of πN rescattering. Whereas MAID employs a K-matrix approximation for the background contribution to the t matrix, DMT includes off-shell contributions in the form of a principal-value integral. Both models use similar Breit-Wigner parametrizations for resonances, but the electroexcitation amplitudes for MAID should be interpreted as "dressed," while for DMT the resonant amplitudes are considered "bare" because the πN rescattering terms account for background contributions to resonant multipoles.

The Sato-Lee (SL) model [60] is formulated in terms of energy-independent effective Hamiltonian and current operators. This dynamic model provides coupled equations for the πN and γN reactions that automatically satisfy unitarity. The potential governing pion rescattering is optimized to reproduce πN elastic scattering data. By means of a unitary transformation, one can distinguish between the electroexcitation amplitudes for the $N \to \Delta$ transition and the contributions of the pion cloud and rescattering mechanisms. Although differing in detail, both the DMT and SL analyses conclude that the pion cloud is responsible for enhancing the M_{1+} amplitude relative to the quark model and for most of the observed quadrupole strength. Thus, these models suggest that the intrinsic deformation is rather small. Note that the SL model omits higher resonances and is limited to $W \lesssim 1.4$ GeV, while the DMT model reaches larger W by including contributions of higher resonances based upon MAID2000.

The data for response functions are compared in Figs. 12–14 with calculations based upon these models. The response functions in the first two columns, described as R type, depend upon real parts of interference products; while those in the last two columns, described as I type, depend upon imaginary parts. Although the first three response functions in column 1 and the last in column 3 have been observed before, the other 12 response functions have been observed for the first time in this experiment. As a general rule, we find that variations among the models are usually greater for I-type than for R-type response functions, although $R_{TT}'^{t}$ also shows significant model dependence. When $W \approx M_\Delta$, R-type responses are largely determined by the relatively well-known multipole amplitudes for the Δ resonance while I-type responses require interference with nonresonant background or tails of nondominant resonances that are constrained less well by previous data. For both types the variations among models are typically smallest for W near and below M_Δ and increase with W above the Δ resonance. By the time we reach $W \sim 1.3$ GeV, variations among models become large even for R-type responses. Above the Δ resonance, the magnitudes for many of the SL response functions decrease faster than the data as W increases, presumably because of neglect of higher resonances. Conversely, some of the DMT response become too strong as W increases, notably R_{L+T}, R_{LT}, and R_{TT}. SAID appears to be the least accurate of these models, especially for LT response functions. We speculate that this problem might be related to the use of pseudoscalar coupling for Born amplitudes. Among these models, MAID2003 seems to provide the best overall description of the data, but none provides a uniformly good fit.

B. Legendre analysis

In the present representation, the response functions should be polynomials in x of relatively low order, especially if the assumption of M_{1+} dominance is valid near the Δ resonance. According to that assumption, one expects R_{TT} to be constant, R_{LT}, R_{LT}', R_{L+T}^n, R_{TT}^n, and R_{TT}^ℓ to be linear, and only $R_{LT}'^{t}$, $R_{TT}'^{\ell}$, and R_{LT}^t to be cubic; the others are expected to be quadratic. Indeed, at $W = 1.23$ GeV, we find that the data for R_{TT} are almost constant and those for R_{LT} are almost linear, with deviations from these simple behaviors that are qualitatively consistent with the departures of the models

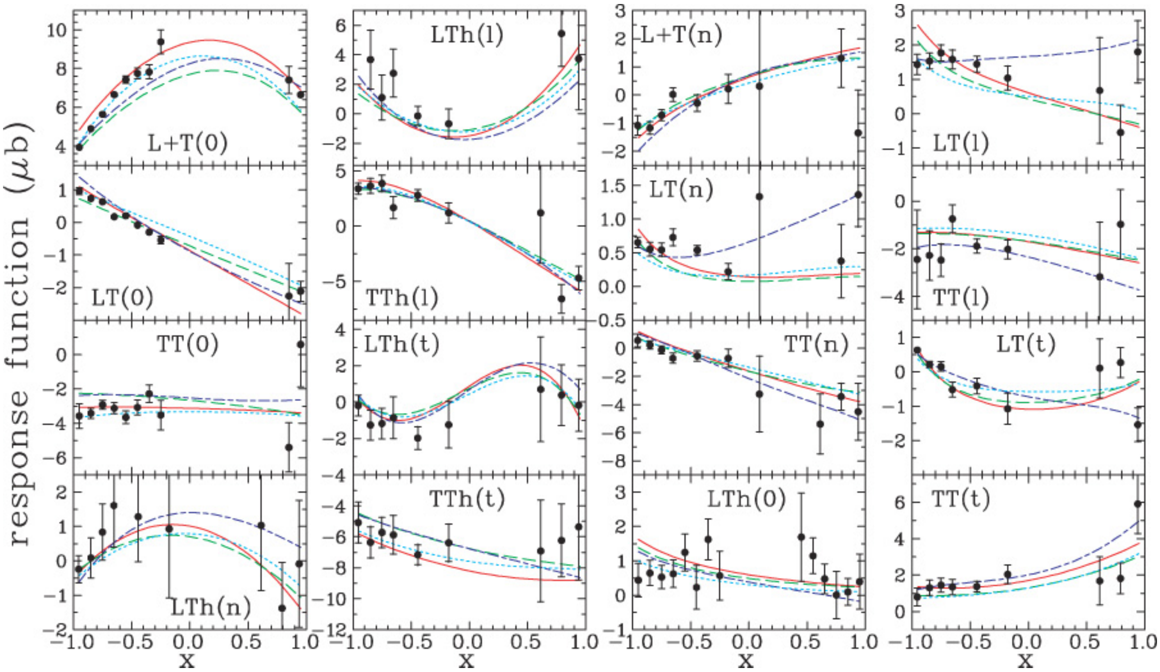

FIG. 12. (Color online) Data for response functions at $W = 1.19$ GeV compared with selected models: MAID2003 (solid red), DMT (dashed green), SAID (dash-dotted blue), and SL (dotted cyan). Inner error bars with end caps are statistical, while outer error bars without end caps include systematic uncertainties; however, the systematic contributions are often indistinguishable.

from M_{1+} dominance. Similarly, at $W = 1.23$ GeV, R'_{LT} and R^n_{TT} appear to be consistent with linear behavior despite the somewhat larger experimental uncertainties. However, model calculations for these responses show larger deviations with respect to M_{1+} dominance because imaginary parts of interference products are more sensitive to nonresonant mechanisms and tails of nondominant resonances. Finally, although R'^n_{LT} displays cubic behavior, R'^{ℓ}_{TT} appears to be almost linear because the $|M_{1+}|^2$ contribution to its linear coefficient dominates the polynomial. However, these simple rules deteriorate rapidly as W increases, and R_{LT}, R^n_{L+T} and R^{ℓ}_{TT} data develop strong curvatures. Furthermore, model

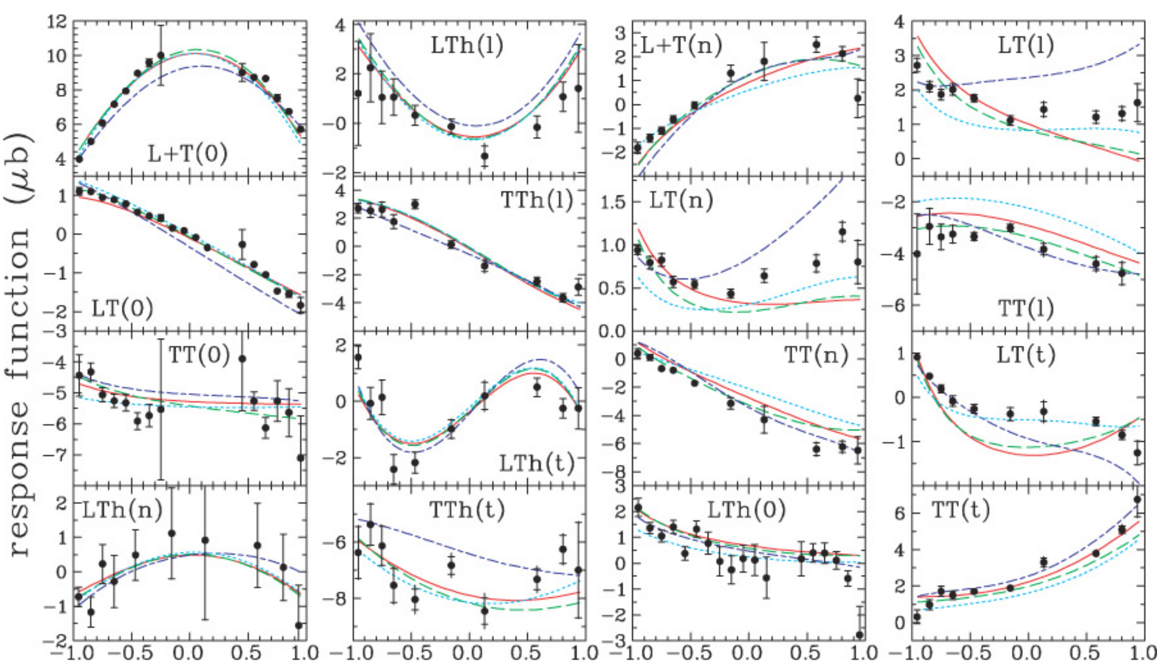

FIG. 13. (Color online) Same as Fig. 12, but for $W = 1.23$ GeV.

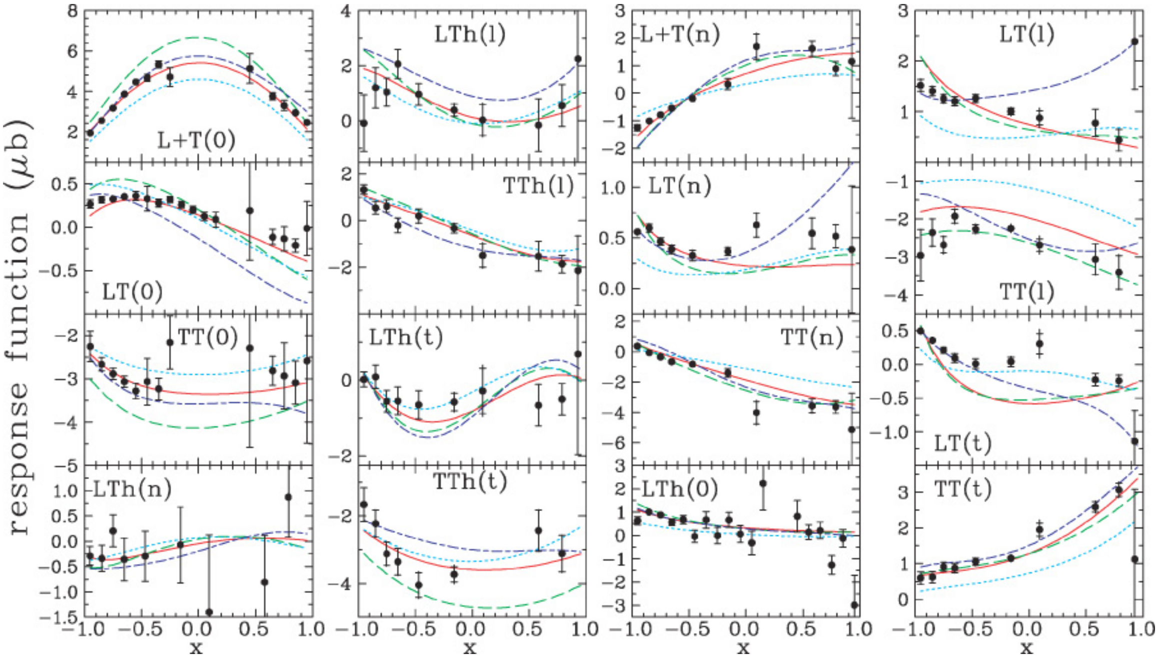

FIG. 14. (Color online) Same as Fig. 12, but for $W = 1.27$ GeV.

calculations also show significant departures from these simple behaviors; for example, the curvature of R_{TT} calculations is often appreciable.

Representative Legendre fits are compared in Figs. 15–17 with data for response functions. A more complete set of figures and comparisons between fitted and predicted Legendre coefficients can be found in Ref. [61]. Note that these fits employed the (x, ϕ) distribution for the differential cross section and beam analyzing power together with the data for recoil polarization response functions. Thus, although R_{L+T} and R_{TT} could not be separated for $x \approx 0$ directly, the Legendre fits to those response functions are determined well in this region nonetheless. The dashed curves are limited to the *sp* truncation, while solid curves include additional terms in response functions for which the *sp* fits appear to be systematically deficient over a range of W. Most of

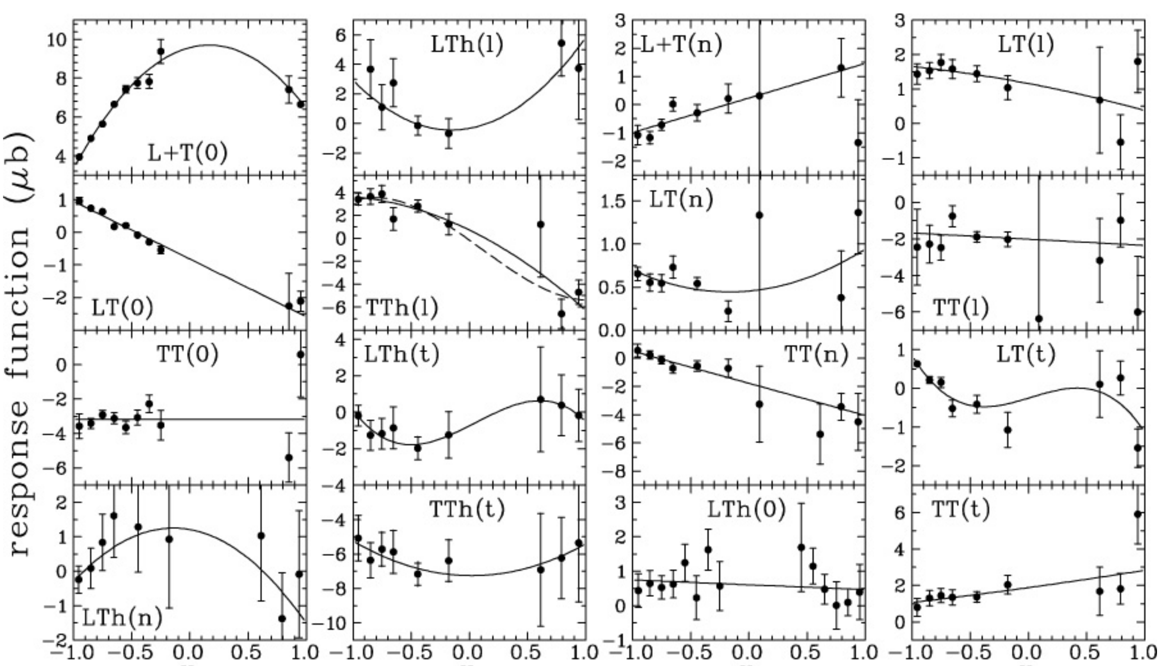

FIG. 15. Data for response functions at $W = 1.19$ GeV compared with Legendre fits in the *sp* truncation (dashed) and with a few extra terms as needed (solid). Inner error bars with end caps are statistical; outer error bars without end caps include systematic uncertainties.

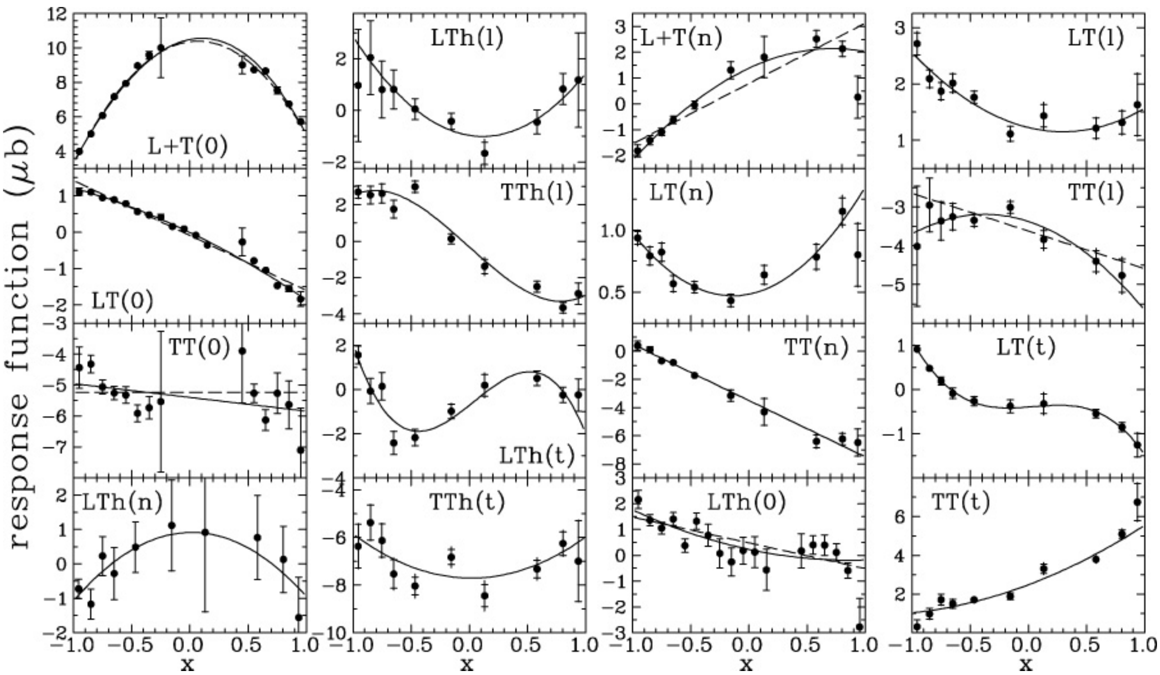

FIG. 16. Same as Fig. 15, but for $W = 1.23$ GeV.

the response functions can be fit well with the truncation based upon M_{1+} dominance, but R_{LT}, R_{TT}, R^n_{L+T}, and R^ℓ_{TT} generally require an extra term that reveals additional contributions. However, it is not immediately obvious whether those additional contributions arise from $\ell_\pi \leqslant 1$ terms that do not involve M_{1+} or whether they require participation of higher partial waves. It is also important to recognize that even when Legendre expansions limited by M_{1+} dominance do fit the data well, considerable violation of this assumption may still be present. Legendre fits are made to the data for each response function independently and ignore the correlations between response functions required by multipole expansions. A detailed study of the truncation errors in the Legendre analysis of unpolarized response functions and their consequences for simplistic extraction of multipole amplitudes is provided in Ref. [74]. Therefore, a more rigorous analysis that fits the multipole amplitudes directly, without the mediation of Legendre coefficients, is presented in Sec. VI C.

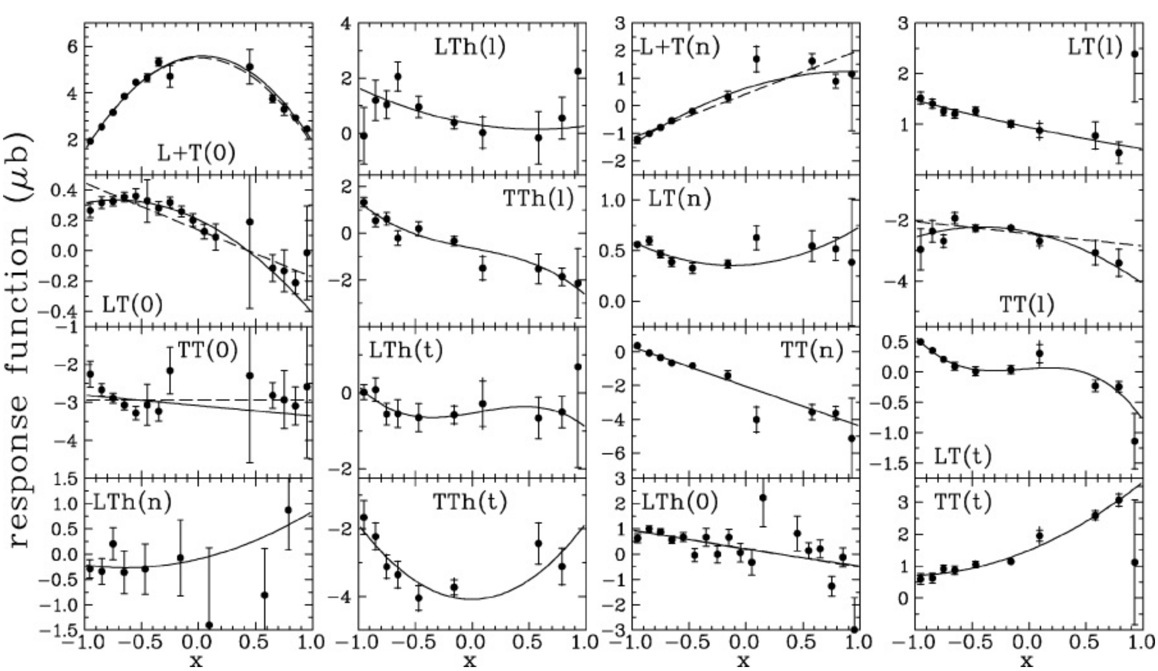

FIG. 17. Same as Fig. 15, but for $W = 1.27$ GeV.

Most previous extractions of $R_{\mathrm{EM}}^{(3/2)}$ and $R_{\mathrm{SM}}^{(3/2)}$ employed truncated Legendre analysis of the unpolarized differential cross section. To the extent that M_{1+} dominance and sp truncation apply for $W \approx M_\Delta$, one can define

$$R_{\mathrm{EM}}^{(p\pi^0)} \approx \tilde{R}_{\mathrm{EM}}^{(p\pi^0)} \qquad R_{\mathrm{SM}}^{(p\pi^0)} \approx \tilde{R}_{\mathrm{SM}}^{(p\pi^0)}, \tag{31}$$

where

$$\tilde{R}_{\mathrm{EM}} = \frac{3A_2^{L+T} - 2A_0^{TT}}{12A_0^{L+T}} \tag{32a}$$

$$\tilde{R}_{\mathrm{SM}} = \frac{A_1^{LT}}{3A_0^{L+T}} \tag{32b}$$

are W-dependent combinations of Legendre coefficients for a particular charge state. To obtain the desired quantities for the $\Delta(1232)$ resonance, these quantities are evaluated at $W = M_\Delta$, and one needs to correct for the isospin 1/2 contamination of the $p\pi^0$ channel. The isospin correction is expected to be small and has not been made. The reliability of Eq. (31) will be evaluated in Sec. VII A.

Figure 18 compares values for $\tilde{R}_{\mathrm{EM}}^{(p\pi^0)}$ and $\tilde{R}_{\mathrm{SM}}^{(p\pi^0)}$ obtained from Legendre fits to the differential cross section data for $Q^2 = 1.0\,(\mathrm{GeV}/c)^2$ with model calculations obtained from Eq. (32), where the Legendre coefficients were obtained by numerical integration. Although these quantities approximate $R_{\mathrm{EM}}^{(p\pi^0)}$ and $R_{\mathrm{SM}}^{(p\pi^0)}$ only for $W \approx M_\Delta$, their W dependence offers some insight into the model dependence of the traditional truncated Legendre expansion. The open circles were obtained using the M_{1+} truncation, while the filled circles vary an additional term for each response function in order to improve the fits for larger W. Recall that Figs. 5–7 demonstrate that the data are sensitive to at least one additional term per response function and that model calculations predict significant Legendre coefficients beyond M_{1+} dominance.

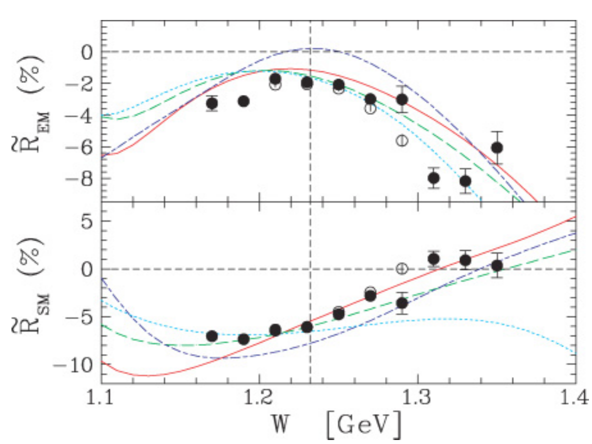

FIG. 18. (Color online) The truncated Legendre analysis for EMR and SMR at $Q^2 = 1.0\,(\mathrm{GeV}/c)^2$ compared with MAID2003 (solid red), DMT (dashed green), SAID (dash-dot blue), and SL (dotted cyan). Both theory and experiment employ Eq. (32) and approximate EMR and SMR at $W = M_\Delta$, indicated by the vertical line. Open circles are fit according to sp truncation; filled circles permit additional freedom in the Legendre analysis. For filled circles, inner error bars with end caps are statistical while outer error bars without end caps include systematic uncertainties.

Although the uncertainties increase for $W > 1.3$ GeV because the angular acceptance becomes too limited, we find that both analyses are qualitatively consistent for an appreciable range of W around M_Δ. The data for these quantities are relatively smooth with W dependencies that are similar to model calculations of the same quantities, whether or not these quantities are adequate approximations to the desired quadrupole ratios.

The spread among models is smallest near the physical mass but remains appreciable for $\tilde{R}_{\mathrm{EM}}^{(p\pi^0)}$, for which SAID differs significantly from both the data and the other models shown. Although the SL slope is somewhat too small compared with data near M_Δ, the other models provide a qualitatively consistent description of the W dependence of $\tilde{R}_{\mathrm{SM}}$. In the central W region, the experimental results are practically independent of truncation scheme and are in reasonable agreement with the MAID or DMT models; but for SAID when $W \approx M_\Delta$, the positive $\tilde{R}_{\mathrm{EM}}$ values disagree sharply with the data. For larger W, the SL calculation for $\tilde{R}_{\mathrm{SM}}$ is much flatter than the data, probably because higher resonances are omitted. Although it is more difficult to obtain unambiguous $\tilde{R}_{\mathrm{EM}}$ results for $W \geqslant 1.31$ GeV, data based upon the sp truncation remain in reasonable agreement with model calculations based upon the same truncation scheme.

The results for $W = 1.23$ GeV are listed in Table II and are practically independent of truncation scheme—the slight variation in $\tilde{R}_{\mathrm{EM}}$ is within the estimated statistical uncertainty. We also list in Table II the values obtained by Joo *et al.* [18] using the sp truncation, averaging with respect to neighboring Q^2 bins. Their results are consistent with ours for $\tilde{R}_{\mathrm{EM}}^{(p\pi^0)}$ but are significantly larger for $\tilde{R}_{\mathrm{SM}}^{(p\pi^0)}$. Note that Joo *et al.* estimated that truncation errors in determination of quadrupole ratios were no more than 0.5% for SMR or 0.7% for EMR in absolute terms. While we agree that truncation of Legendre fits to the number of terms in the sp model has little effect upon fitted values for $\tilde{R}_{\mathrm{EM}}$ or $\tilde{R}_{\mathrm{SM}}$, the discussion in Sec. VII demonstrates that the underlying assumptions of the traditional Legendre analysis do not provide adequate approximations to the quadrupole ratios at the present level of experimental precision. Therefore, the next section presents a more rigorous analysis based upon multipole fits that does not assume sp truncation or M_{1+} dominance.

This analysis for the quadrupole ratios is based upon unpolarized cross sections and does not exploit any of the new recoil polarization data. Many combinations of Legendre amplitudes

TABLE II. Legendre analysis of quadrupole ratios for $W = 1.23$ GeV at $Q^2 = 1.0\,(\mathrm{GeV}/c)^2$. The reduced chi-square for the entire data set is χ^2_ν; the chi-square per point for differential cross section data is $\chi^2_N(\sigma)$.

Method	SMR (%)	EMR (%)	χ^2_ν	$\chi^2_N(\sigma)$
sp	-6.07 ± 0.11	-2.04 ± 0.13	1.7	1.6
$sp+$	-6.11 ± 0.11	-1.92 ± 0.14	1.5	1.4
Joo *et al.*[a]	-7.4 ± 0.4	-1.8 ± 0.4		

[a]Weighted average of $Q^2 = 0.9\,(\mathrm{GeV}/c)^2$ results for $E_i = 1.645$ and 2.445 GeV from Ref. [18].

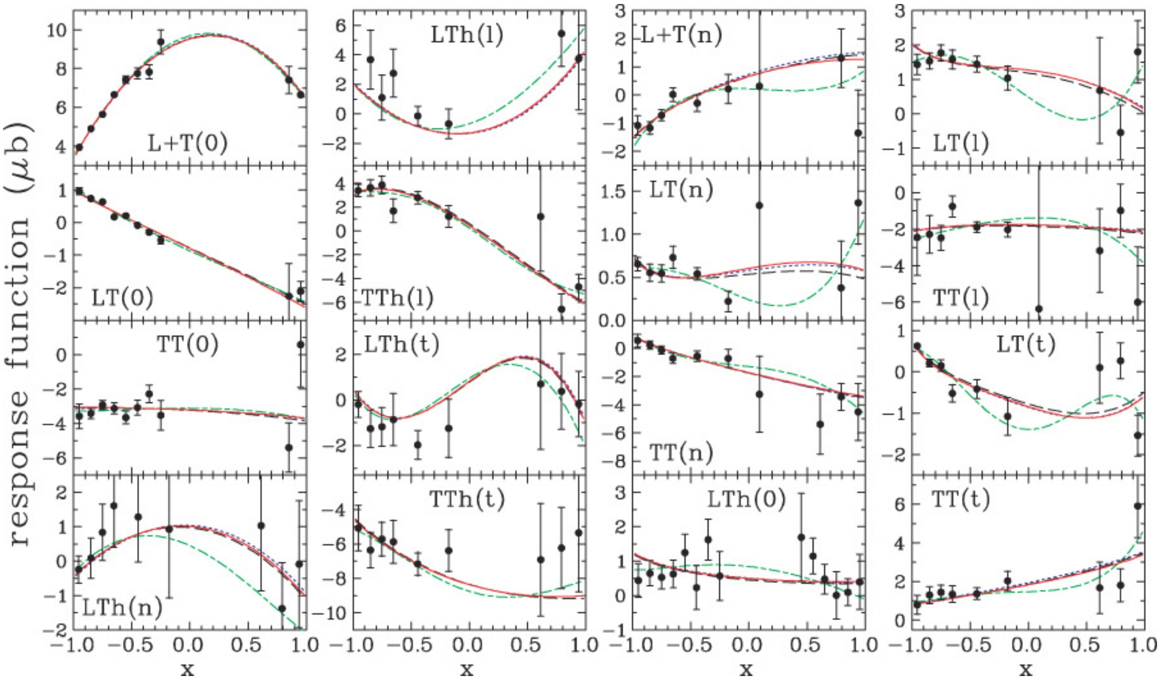

FIG. 19. (Color online) Multipole fits for $W = 1.19$ GeV at $Q^2 = 1.0\,(\mathrm{GeV}/c)^2$ using a Born baseline model. Dashed curves fit corrections to all s- and p-wave amplitudes, blue dotted curves also fit real parts of $2-$ multipoles, and green dash-dotted curves fit all s-, p-, and d-wave amplitudes. The solid red curves, considered the final fit, are similar to the blue dotted curves except that $\mathrm{Im}M_{1-}$ is absent. See text for further details.

for polarized responses could also provide $\mathrm{Re}E_{1+}M_{1+}^*$ and $\mathrm{Re}S_{1+}M_{1+}^*$—if the sp truncation is valid these quantities should be highly overdetermined. Thus, one could obtain $\mathrm{Re}E_{1+}M_{1+}^*$ and $\mathrm{Re}S_{1+}M_{1+}^*$ using a least-squares analysis of the entire set of Legendre coefficients for $W = M_\Delta$ and measure the reliability of the truncation scheme by χ^2. However, it is already clear from the Legendre fits that terms beyond sp truncation are needed for some of the response functions even for $W \approx M_\Delta$. Furthermore, it is desirable to obtain the W dependencies of both the real and the imaginary parts of the multipole amplitudes. Therefore, we forgo further study of the consistency of sp truncation and proceed directly to a multipole analysis that exploits the new response functions.

C. Multipole analysis

Let

$$A_i(W, Q^2) = A_i^{(0)}(W, Q^2) + \Delta A_i(W, Q^2) \qquad (33)$$

represent either the real or the imaginary part of one of the multipole amplitudes ($M_{\ell j}$, $E_{\ell j}$, or $S_{\ell j}$) where $A_i^{(0)}$ is a baseline amplitude obtained from a suitable model while ΔA_i is a variable to be fit to the data. To minimize theoretical bias, our standard fits employ a baseline model consisting of Born terms for pseudovector πNN coupling plus ρ and ω exchange; see the Appendix for details. To test the sensitivity of fitted multipole amplitudes to neglect of tails of nondominant resonances or to variations of nonresonant contributions, we have also performed fits using MAID2003, DMT, SL, or SAID as baseline models. Note that some of the ΔA_i parameters are relatively large when using the Born baseline that contains no information about the $\Delta(1232)$ resonance, while the fitting parameters for more sophisticated baseline models represent small corrections to the specified model. Nevertheless, we have demonstrated that fitted multipole amplitudes are practically independent of the baseline model; see Ref. [62] for details and figures. Both Legendre and multipole analyses were performed using the EPIPROD program [75].

Fits were performed for each W bin to data consisting of the (x, ϕ) distributions of differential cross section and beam analyzing power plus x distributions for 12 recoil polarization response functions simultaneously. Fits using Born amplitudes for pseudovector coupling as the baseline model are shown in Figs. 19–21. Several fits were performed to determine the maximum number of parameters that could be extracted without flattening the χ^2 hypersurfaces too severely or encountering uncontrollable correlations among parameters. Dashed curves, designated sp, show fits that adjust real and imaginary parts of all s- and p-wave multipole amplitudes with higher partial waves constrained by the baseline model, here just real Born amplitudes without resonances. The fits designated $spd3$ also vary the real parts of $2-$ multipoles and are shown as blue dotted curves. Fits designated spd vary real and imaginary parts of all amplitudes with $\ell_\pi \leqslant 2$ and are shown as green dash-dotted curves. Finally, the fits designated "final" are similar to the $spd3$ fits except that $\mathrm{Im}M_{1-}$ is held at baseline, here zero, for reasons discussed below. There are 14 free parameters for each W in an sp fit, 26 for an spd fit, 17 for an $spd3$ fit, and 16 for the final fit. For comparison, Legendre fits vary 50 free parameters in the central W region.

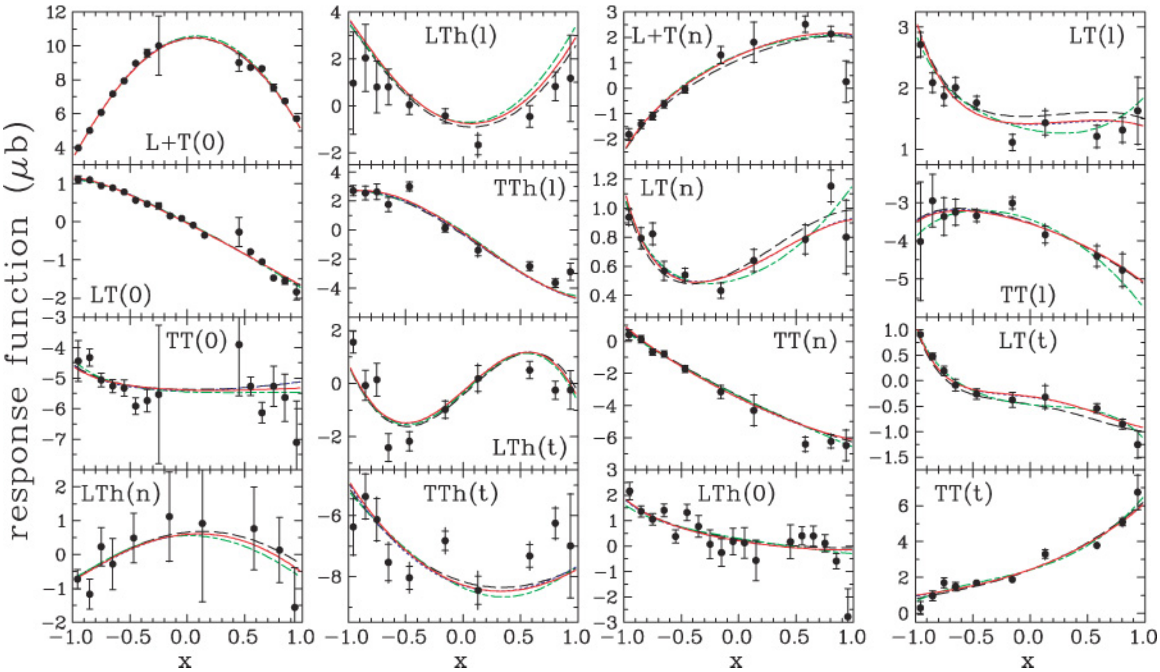

FIG. 20. (Color online) Same as Fig. 19, but for $W = 1.23$ GeV at $Q^2 = 1.0\,(\text{GeV}/c)^2$.

These figures show that fitting just the s- and p-wave amplitudes, with a Born background, is already sufficient to obtain a good description of the data. Although fitting d-wave amplitudes, or a subset thereof, sometimes provides modest reductions of χ^2, there is little systematic evidence that modification of d-wave or higher multipoles is really necessary. However, it is also clear that variation of all $\ell_\pi \leqslant 2$ amplitudes offers too much freedom—the oscillations in green dash-dotted curves for $W \geqslant 1.29$ GeV or $W \leqslant 1.19$ GeV are not needed to fit the data, are implausible in amplitude, and change too much from one W to the next.

The fitted multipole amplitudes are compared in Figs. 22–26 with several recent models [49,60,73,76]. In addition, the baseline Born amplitudes are shown by solid curves. Note that all multipole amplitudes are real in this model, and there are no resonances; therefore, the starting conditions are quite poor, and large adjustments to the initial parameters are required to fit the data. Nevertheless, the fits

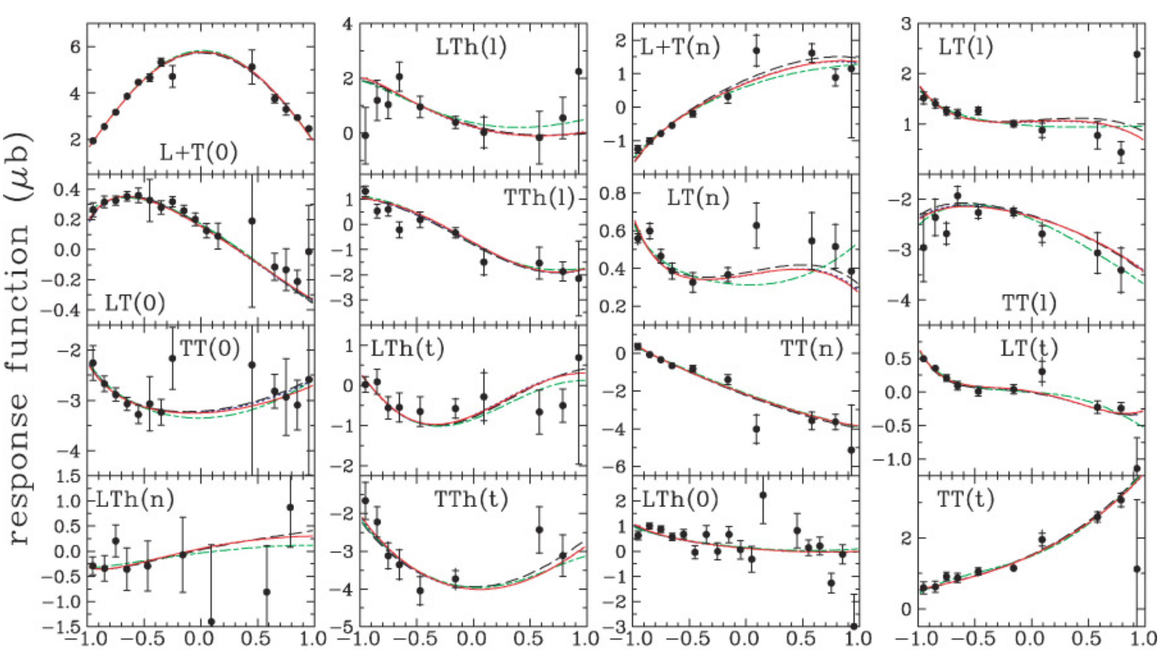

FIG. 21. (Color online) Same as Fig. 19, but for $W = 1.27$ GeV at $Q^2 = 1.0\,(\text{GeV}/c)^2$.

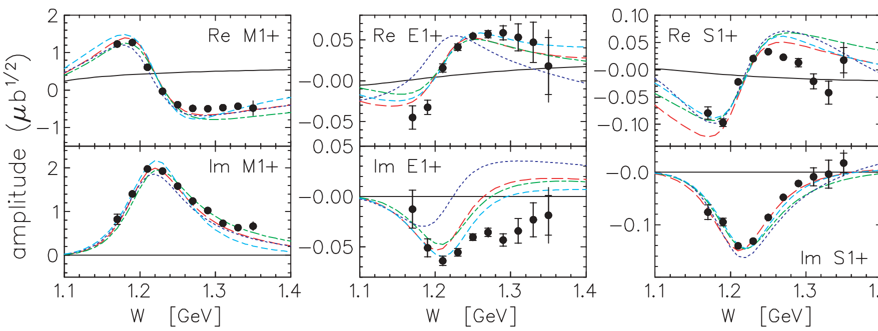

FIG. 22. (Color online) Fitted 1+ multipole amplitudes using Born baseline and adjusting all ℓ_π amplitudes except ImM_{1-} plus real parts of 2− amplitudes. Inner error bars with end caps are statistical; outer error bars without end caps include systematic uncertainties. The baseline amplitudes are shown as black curves. Other models shown are MAID2003 (red dashed), DMT (green dot-dashed), SAID (blue dotted), and SL (cyan short-dashed).

describe the data well, the fitted parameters generally display smooth W dependencies, and the characteristic resonance profiles emerge in the 1+ multipole amplitudes without coaching. Note that the *sp* and final fits began with baseline amplitudes, but to improve stability the fits with more freedom began with the results of the final analysis. The uncertainties increase with the number of free parameters because the data do not adequately constrain multipoles for $\ell_\pi \geqslant 2$. Thus, we reject the full *spd* analysis because the uncertainties in its parameters are large and the resultant oscillations in calculated response functions are not warranted by the available data. The amplitudes and resulting fits for the other three analyses tend to be very similar except that there is a rather strong correlation between ImM_{1-} and ImS_{1-} for small W that results in fitted values of opposite sign that are substantially larger than model predictions for $W \leqslant 1.21$ GeV. This correlation also appears to affect imaginary parts of 1+ amplitudes for $W = 1.17$ GeV. Evidently, the data for low W do not distinguish between ImM_{1-} and ImS_{1-} well enough to fit both simultaneously. Therefore, our final analysis eliminates ImM_{1-} because models tend to predict stronger ImS_{1-} amplitudes and the *sp* fit also produces rather small ImM_{1-} values. The uncertainties in fitted multipoles is reduced and the W dependencies are improved, especially for imaginary 1+ amplitudes, upon elimination of this redundant parameter. Furthermore, Figs. 19–21 demonstrate that elimination of ImM_{1-} does not visibly reduce the quality of the fits to the data. The "final" analysis varies both real and imaginary parts of S_{1-} and all 0+ and 1+ multipoles plus the real parts of M_{1-} and all 2− multipoles for a total of 16 free parameters for each (W, Q^2) bin.

There is rather little spread among models for M_{1+} amplitudes across the $\Delta(1232)$ resonance, and our experimental amplitudes agree well with model calculations even when the fit is based upon a Born baseline model without resonances. The variation among models is also relatively small for S_{1+} amplitudes, and good agreement is obtained with data for ImS_{1+}, but for the real part the present data exhibit a steeper slope on the large W side. MAID2003, DMT, and SL calculations are similar for E_{1+}, but the current SAID calculations are substantially different and disagree with the data. Our results for ReE_{1+} agree relatively well with MAID2003, DMT, or SL but the ImE_{1+} data do not show the node near $W \approx 1.27$ GeV predicted by those models; there is no sign change for $W \leqslant 1.35$ GeV.

Among the models considered, MAID2003 tends to provide the best description of the recoil polarization data, but it does not reproduce the R^{ℓ}_{LT}, R^{t}_{LT}, or R^{n}_{LT} angular distributions (see Figs. 12–14). These difficulties appear to arise primarily from the S_{0+} amplitudes. Whereas MAID2003 suggests a nearly constant ReS_{0+} amplitude in this W range, we find less negative results that are consistent with the negative slope in W suggested by SAID. Although the SL calculation crosses the ReS_{0+} data near the middle of the W range, it has the opposite slope. We also find a rather steep slope for ImS_{0+}. It is interesting to observe that the SAID model agrees best with the 0+ amplitudes even though it is worst, among these models, for E_{1+}, Re1−, and S_{2-}. All of the models agree pretty well with the ReE_{0+} data, but none reproduces the W dependence seen for ImE_{0+}.

It is interesting to observe that there is a wide spread among the models for ReM_{1-} but that the data are closest to the Born model that omits the Roper resonance, which suggests that the transverse amplitude ${}_pA_{1/2}$ is small. On the other hand, the fitted ReS_{1-} does differ from the Born model and suggests

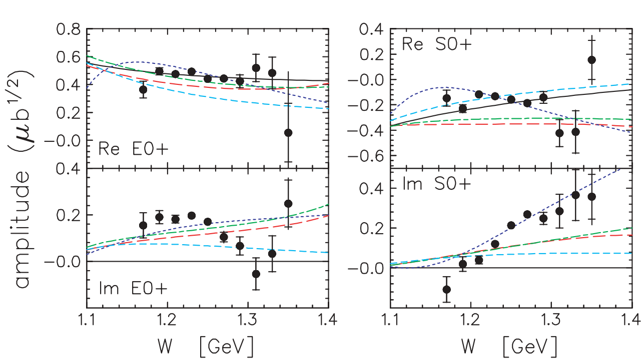

FIG. 23. (Color online) Same as Fig. 22, but for 0+ multipole amplitudes.

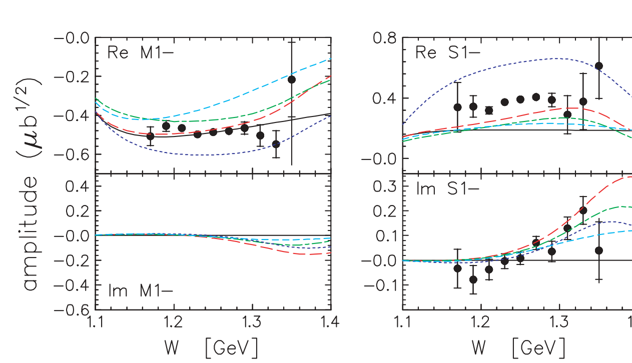

FIG. 24. (Color online) Same as Fig. 22, but for 1− multipole amplitudes.

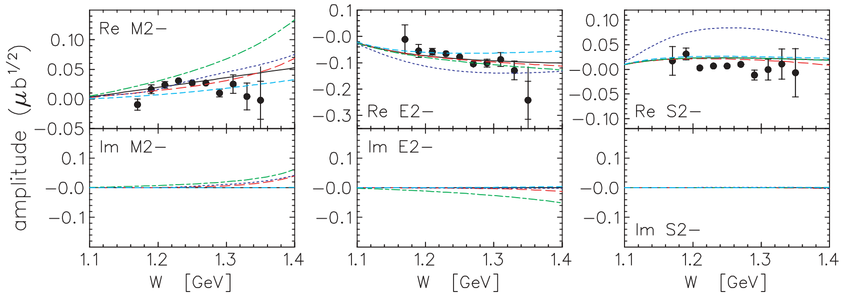

FIG. 25. (Color online) Same as Fig. 22, but for 2− multipole amplitudes.

that there is a nonnegligible longitudinal contribution from the Roper consistent with a radial excitation. These models agree fairly well with the ImS_{1-} data but, with the exception of the large SAID prediction, are smaller than the ReS_{1-} data. Thus, it appears that excitation of the Roper resonance is primarily longitudinal at $Q^2 = 1\,(\text{GeV}/c)^2$.

The real 2− amplitudes are small in this W range, but the slope for ReE_{2-} appears to be determined well by these data and is in good agreement with Born, MAID2003, or DMT predictions. However, the predictions of the SAID model are much larger than the data for ReS_{2-}. SAID also predicts significant oscillations in 2+ amplitudes that are absent in other models. Although we cannot fit the 2+ amplitudes accurately, the large $\ell_\pi = 2$ amplitudes for SAID produce oscillations in many of the response functions that are not warranted by the data.

D. Quadrupole ratios

The quadrupole deformation parameters can now be obtained directly from the fitted multipole amplitudes using

$$\mathrm{Re}\frac{E_{1+}}{M_{1+}} = \frac{\mathrm{Re}E_{1+}M_{1+}^*}{|M_{1+}|^2} = \frac{\mathrm{Re}E_{1+}\mathrm{Re}M_{1+} + \mathrm{Im}E_{1+}\mathrm{Im}M_{1+}}{\mathrm{Re}M_{1+}\mathrm{Re}M_{1+} + \mathrm{Im}M_{1+}\mathrm{Im}M_{1+}}, \tag{34a}$$

$$\mathrm{Re}\frac{S_{1+}}{M_{1+}} = \frac{\mathrm{Re}S_{1+}M_{1+}^*}{|M_{1+}|^2} = \frac{\mathrm{Re}S_{1+}\mathrm{Re}M_{1+} + \mathrm{Im}S_{1+}\mathrm{Im}M_{1+}}{\mathrm{Re}M_{1+}\mathrm{Re}M_{1+} + \mathrm{Im}M_{1+}\mathrm{Im}M_{1+}}. \tag{34b}$$

where the multipole analysis provides the real and imaginary parts of each amplitude separately. The W dependencies of quadrupole ratios for the $p\pi^0$ channel are shown in Fig. 27 and the results at $W = 1.23$ GeV are listed in Table III; the correction for the small isospin 1/2 contamination is discussed in Sec. VII. The truncation dependence of the experimental results is relatively small for $R_{\rm SM}^{(p\pi^0)}$, and most of the models are in good agreement with the data for $W \approx M_\Delta$, but SMR is significantly stronger for SAID. Although the truncation dependence is larger for $R_{\rm EM}^{(p\pi^0)}$ data, the value at M_Δ still appears to be determined relatively well and is consistent with all the models except SAID, which gives a much smaller value and at larger Q^2 sign opposite other models. The model calculations spread more rapidly for the electric than for the scalar ratio as the distance from M_Δ increases.

Note that if one defines M_Δ as the W where Re$M_{1+}^{(3/2)} = 0$, then the quadrupole formulas in Eq. (34) reduce to

$$R_{\rm EM}^{(3/2)} = \mathrm{Im}E_{1+}^{(3/2)}/\mathrm{Im}M_{1+}^{(3/2)} \tag{35a}$$

$$R_{\rm SM}^{(3/2)} = \mathrm{Im}S_{1+}^{(3/2)}/\mathrm{Im}M_{1+}^{(3/2)} \tag{35b}$$

for the isospin 3/2 channel. However, these formulas are unsuitable for data analysis because comparable $n\pi^+$ data are not available for isospin decomposition and because the appropriate value of M_Δ is not known precisely or independently of models. It would also be necessary, in principle, to interpolate the multipole data with respect to W. We employ Eq. (34) because it is independent of W, applies equally well to $p\pi^0$ or isospin 3/2, and does not require any model-dependent assumptions about M_Δ. Furthermore, because the energy dependence in Fig. 27 is quite mild, Table III simply lists values for the bin closest to M_Δ, namely, $W = 1.23$ GeV. Small corrections for the energy dependence of these quantities are evaluated in Sec. VII C.

Table III evaluates the sensitivity of quadrupole ratios to the selection of adjustable multipoles. The uncertainties increase when higher partial waves that are not well-constrained by the data are permitted to vary. Above we argued that the best compromise is obtained by varying 0+, 1+, 1−, and real parts of 2− multipole amplitudes with 2+ and higher partial waves constrained by the baseline model. Elimination of ImM_{1-} further reduces the uncertainties in SMR, without affecting the quality of the fit, by suppressing its unresolvable correlation with ImS_{1-}. As previously argued, we believe that elimination

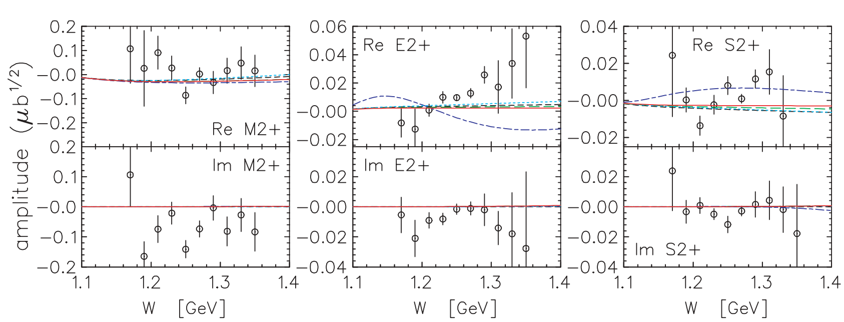

FIG. 26. (Color online) Same as Fig. 22, but for 2+ multipole amplitudes. The open circles show results for the *spd* analysis. Only statistical errors are shown.

TABLE III. Quadrupole ratios for $W = 1.23$ GeV at $Q^2 = 1.0\,(\mathrm{GeV}/c)^2$ using the pseudovector Born baseline model. Only statistical uncertainties from fitting are given.

Variables	SMR (%)	EMR (%)	χ^2_ν
0+, 1+, 1−	-6.73 ± 0.24	-2.43 ± 0.19	1.69
0+, 1+, 1−, 2−, 2+	-6.95 ± 0.49	-3.19 ± 0.79	1.64
0+, 1+, 1−, Re2−	-6.85 ± 0.27	-2.73 ± 0.20	1.65
Above, except ImM_{1-}	-6.84 ± 0.15	-2.91 ± 0.19	1.65

of ImM_{1-} is justified by the prediction—made by all models considered—that it is negligible in this energy range. The results in the last two lines of Table III are practically identical for SMR, though with reduced uncertainty in the final line, while the change in EMR is within the estimated uncertainties.

E. Sensitivity to baseline model

As mentioned above, the multipole fits are rather insensitive to the choice of baseline model. To illustrate this, Fig. 28 compares fits to the response functions for $W = 1.23$ GeV based upon several baseline models; figures for other W bins are available in Ref. [62]. The fits based upon Born, MAID2003, DMT, or SL models are practically indistinguishable. The fits based upon SAID display a more oscillatory structure that is not supported by the data in the middle of the W range where the precision is best. The oscillations are presumably due to relatively large ReE_{2+} and ReS_{2+} amplitudes that are not ameliorated by the current truncation scheme. Therefore, the data clearly require smaller 2+ amplitudes than predicted by the SAID model.

Similarly, the fitted multipole amplitudes are also rather insensitive to the choice of baseline model. Even the fits based upon SAID, starting from rather different initial conditions and with significantly larger fixed 2+ amplitudes, converge upon essentially the same final results. For example, Table IV lists the quadrupole ratios for $W = 1.23$ GeV based upon several choices of baseline models and using the "final" parameter

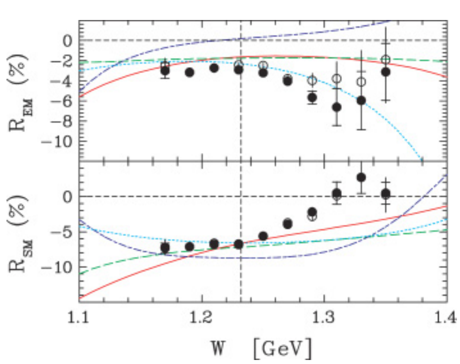

FIG. 27. (Color online) Multipole analyses for EMR and SMR at $Q^2 = 1.0\,(\mathrm{GeV}/c)^2$ are compared with MAID2003 (solid red), DMT (dashed green), SAID (dash-dot blue), and SL (dotted cyan). The vertical line shows the physical mass, $W = M_\Delta$. Open circles adjust $\ell_\pi \leqslant 1$ multipoles; filled circles represent the final fits. For filled circles, inner error bars with end caps are statistical, while outer error bars without end caps include systematic uncertainties.

TABLE IV. Dependence of quadrupole ratios for $W = 1.23$ GeV at $Q^2 = 1.0\,(\mathrm{GeV}/c)^2$ upon baseline model. All s- and p-wave amplitudes, except ImM_{1-}, plus real 2− amplitudes were fit with other amplitudes given by the specified baseline model.

Baseline	SMR (%)	EMR (%)	χ^2_ν
Born	-6.84 ± 0.15	-2.91 ± 0.19	1.65
MAID2003	-6.90 ± 0.15	-2.79 ± 0.19	1.67
DMT	-6.82 ± 0.15	-2.70 ± 0.19	1.67
SL	-6.79 ± 0.15	-2.81 ± 0.19	1.64
SAID	-7.38 ± 0.15	-2.53 ± 0.20	1.85

space. All of the results are consistent except those using the SAID baseline, for which SMR is substantially higher and EMR lower than for other baseline models. However, the quality of the fit is also noticeably inferior even though the differences in χ^2_ν are not impressive. Therefore, we conclude that this version of the SAID model does not provide a suitable baseline for multipole analysis, and we judge the sensitivity to uncertainties in the baseline model to be similar to the tabulated fitting uncertainties.

VII. DISCUSSION

A. Reliability of traditional Legendre analysis

Both the Legendre and multipole analyses fit the data well, but they yield significantly different estimates of the $N \to \Delta$ quadrupole ratios. The Legendre results are listed in the first line of Table V, and those for the multipole analysis in the second and fifth columns of the second line. Subsequent lines show model calculations for quadrupole ratios based upon several truncation schemes. The second and fifth columns are the proper ratios of multipole amplitudes, while the remaining columns use the traditional estimators given by Eq. (32) with Legendre coefficients that were computed by numerical integration of response functions obtained from the indicated truncation of the multipole amplitudes with respect to ℓ_π. Thus, the third and sixth columns represent the sp truncation, while the fourth and seventh columns are practically complete with respect to ℓ_π. We placed the experimental Legendre results in the $\ell_\pi \leqslant 5$ columns because truncation is not possible experimentally. The model Legendre coefficients were computed without using M_{1+} dominance, but the corresponding traditional quadrupole estimators, $\tilde{R}_{\mathrm{SM}}$ and $\tilde{R}_{\mathrm{EM}}$, employ

TABLE V. Calculated quadrupole ratios (in %) for $W = 1.23$ GeV at $Q^2 = 1.0\,(\mathrm{GeV}/c)^2$. Columns with ranges of ℓ_π are based upon traditional estimators given by Eq. (32).

Model	$R_{\mathrm{SM}}^{(p\pi^0)}$	$\tilde{R}_{\mathrm{SM}}^{(p\pi^0)}$ $\ell_\pi \leqslant 1$	$\tilde{R}_{\mathrm{SM}}^{(p\pi^0)}$ $\ell_\pi \leqslant 5$	$R_{\mathrm{EM}}^{(p\pi^0)}$	$\tilde{R}_{\mathrm{EM}}^{(p\pi^0)}$ $\ell_\pi \leqslant 1$	$\tilde{R}_{\mathrm{EM}}^{(p\pi^0)}$ $\ell_\pi \leqslant 5$
Legendre fit			−6.11			−1.92
Multipole fit	−6.84	−6.46	−6.00	−2.91	−1.54	−2.18
MAID2003	−6.73	−6.37	−5.63	−1.65	−0.57	−1.12
DMT	−7.21	−6.77	−6.10	−1.77	−0.70	−1.47
SAID	−8.71	−7.78	−7.88	+0.17	+1.96	+0.22
SL	−6.59	−6.69	−6.58	−2.29	−1.29	−1.58

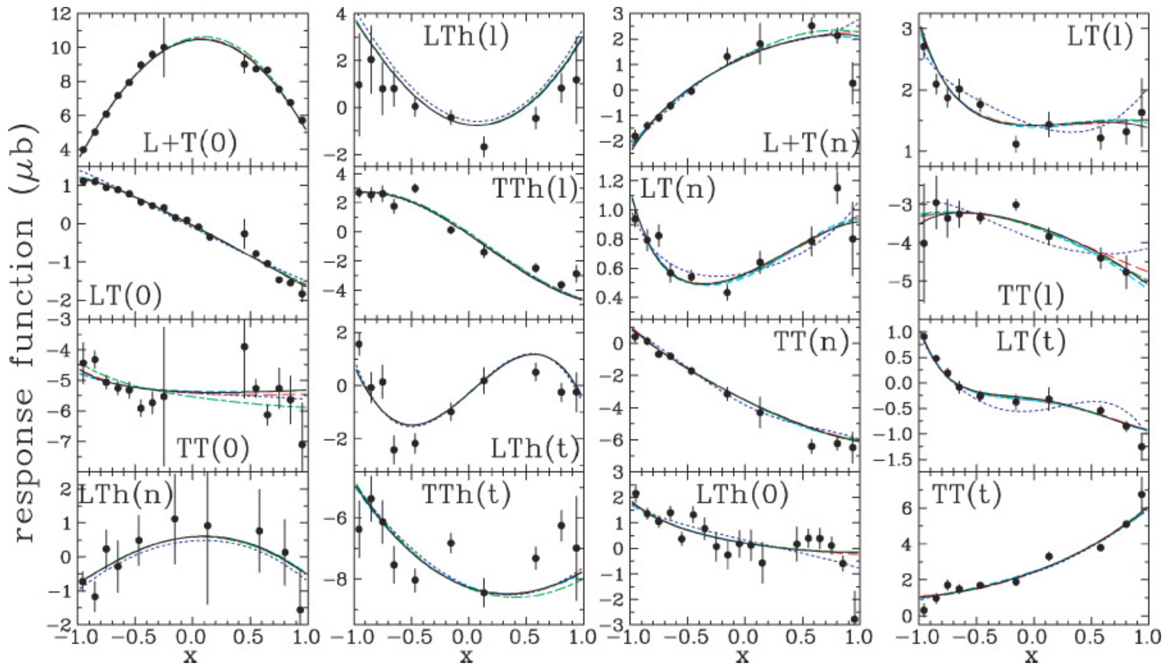

FIG. 28. (Color online) Sensitivity of multipole fits for $W = 1.23$ GeV at $Q^2 = 1.0\,(\mathrm{GeV}/c)^2$ to the choice of baseline model: Born (black solid), MAID2003 (red dashed), DMT (green dash-dotted), SAID (blue dotted), or SL (cyan short-dotted).

combinations that were derived under that assumption. The values of $\tilde{R}_{\mathrm{SM}}$ and $\tilde{R}_{\mathrm{EM}}$ for $\ell_\pi \leqslant 5$ obtained from the fitted multipole amplitudes are similar to those obtained from the fitted Legendre coefficients but are distinctly smaller than the fitted values for R_{SM} and R_{EM} even though the fits to the cross section data are practically identical. The differences between $\ell_\pi \leqslant 1$ and $\ell_\pi \leqslant 5$ model calculations demonstrate that *sp* truncation is often a poor approximation to $\tilde{R}_{\mathrm{SM}}$ and $\tilde{R}_{\mathrm{EM}}$, especially for the latter. Although the *sp* truncation of $\tilde{R}_{\mathrm{SM}}$ is reasonable for the SAID and SL models and for the present multipole fit, it is inaccurate for the MAID2003 and DMT models. However, *sp* truncation of $\tilde{R}_{\mathrm{EM}}$ is quite poor for all models considered. Furthermore, the correspondence between the traditional Legendre estimators and the actual quadrupole ratios also depends upon the requirement that M_{1+} appear in every term of the multipole expansion of Legendre coefficients. The differences between the $\ell_\pi \leqslant 5$ results and the actual quadrupole ratios demonstrate that the assumption of M_{1+} dominance is not sufficiently accurate either.

A more detailed study of truncation errors in the traditional Legendre analysis of $N \to \Delta$ quadrupole ratios has been provided in Ref. [74]. Truncation errors are especially severe for $\tilde{R}_{\mathrm{EM}}$ where the contribution of $\mathrm{Re}M_{1-}E^*_{1+}$ alone is approximately -40% of the leading term using MAID2003 $p\pi^0$ multipoles for our kinematics. Many other neglected terms are significant, and the convergence is slow and model dependent. Furthermore, the contributions of A_0^L and A_2^L to Eq. (32) are not negligible, as assumed using M_{1+} dominance. The contribution of A_2^L can, in fact, have a large effect upon delicate cancellations within the numerator of $\tilde{R}_{\mathrm{EM}}$. Thus, Rosenbluth separation should be performed before using the Legendre method, especially for $\tilde{R}_{\mathrm{EM}}$, but none of the recent Legendre analyses [17–19,21] have done so, including the present experiment. The convergence of $\tilde{R}_{\mathrm{SM}}$ is better, but its relative accuracy as an estimate of R_{SM} is still no better than about 20% [74]. Therefore, although the details are model dependent, it is clear that neither assumption of the traditional Legendre analysis is sufficiently accurate at the present levels of experimental precision and completeness.

B. Isospin 1/2 contamination of EMR and SMR

Separation of the isospin 1/2 and 3/2 contributions to the multipole amplitudes would require comparable data for the $n\pi^+$ channel, including angular distributions for either recoil or target polarization, which are presently unavailable. Fortunately, the isospin 1/2 contamination is expected to have relatively little effect upon the determination of isospin 3/2 quadrupole ratios. According to MAID2003, one expects $(R_{\mathrm{SM}}, R_{\mathrm{EM}}) = (-6.71\%, -1.62\%)$ at $(W, Q^2) = (1.23, 1.0)$ for isospin 3/2 compared with $(-6.73\%, -1.65\%)$ for the $p\pi^0$ channel [49]. Similarly, the quadrupole ratios for the pure $N \to \Delta$ contribution become $(-6.73\%, -1.53\%)$ in the absence of background. Finally, if one attributes the correction terms for 1+ multipoles in Eq. (33) entirely to the Δ resonance, assuming that the Born baseline model is accurate, we would estimate

$$R_{\mathrm{SM}}^{(3/2)} \approx \mathrm{Re}\frac{\Delta S_{1+}}{\Delta M_{1+}} = -6.81\%, \tag{36a}$$

$$R_{\mathrm{EM}}^{(3/2)} \approx \mathrm{Re}\frac{\Delta E_{1+}}{\Delta M_{1+}} = -3.12\%, \tag{36b}$$

in good agreement with the full results for the $p\pi^0$ channel that include background. However, the fact that changes in R_{EM} due to neglect of background are opposite for MAID2003,

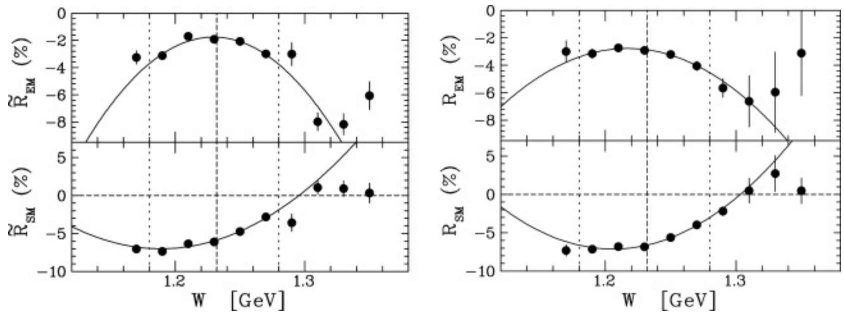

FIG. 29. Parabolic fits to the W dependence of quadrupole ratios from Legendre (left) and multipole (right) analyses. Vertical dashed and dotted lines show M_Δ and the fitted ranges of W.

and the experimental multipole fit suggests that part of the fitted ΔE_{1+} should probably be attributed to the background in the baseline model. Nevertheless, it appears that corrections for isospin 1/2 contamination are probably smaller than the present error bars. Therefore, this model-dependent correction has not been made.

C. W dependence of EMR and SMR

The W dependencies of quadrupole ratios obtained using both Legendre and multipole analyses are compared in Fig. 29 with parabolic fits of the form

$$y = \sum_{k=0}^{2} a_k (W - M_\Delta)^k, \tag{37}$$

using a nominal value of $M_\Delta = 1.232$ GeV. The fits were confined to the central region, indicated by dotted vertical lines, where this simple parametrization should suffice for interpolation. Both fits describe the data for the central region well. It is important to remember that the quadrupole ratios for the two types of analysis are different quantities and need not have the same shapes—the Legendre estimators are affected by ϵ and by all partial waves while those from multipole analysis are not. The parabolic fits appear to extrapolate better for the multipole analysis than for the Legendre analysis, but they should still only be used in the central region.

The expansion coefficients fitted using the weighted linear least-squares method are given in Table VI, where the data for quadrupole ratios are expressed in percent and the multipole amplitudes are based upon the Born baseline. The a_0 parameters represent best-fit estimates of the quadrupole ratios at M_Δ, but fits with only 2 degrees of freedom do not necessarily provide realistic uncertainties. Instead, we quote the largest of $\delta R(1.23)$, δa_0, and $\delta a_0 \sqrt{\chi^2_\nu}$, where $\delta R(1.23)$ is the uncertainty in the single-energy fit to data for $W = 1.23$ GeV, δa_0 is the uncertainty in the value of a_0 according to the linear least-squares fit to the energy dependence, and χ^2_ν is the reduced chi-square for that fit in the central region. The second-order terms are negligible between M_Δ and the nearest W bin, and changes due to the linear terms are less than one standard deviation. For example, the fitted EMR and SMR values for the multipole analysis are -2.85% and -6.69% at $W = 1.23$ GeV. The remaining differences between these values and those listed on the last line of Table III are less than one standard deviation. Although the quadrupole ratios in Table VI are slightly smaller, they are consistent with those we reported in Ref. [33]. The analysis in Ref. [33] considered only a single energy, $W = 1.23$ GeV, while the present analysis fits the energy dependence within the central region. The small differences are partly due to the change in W from 1.23 to 1.232 GeV and partly due to statistical fluctuations of the data for 1.23 GeV relative to the average trends represented by the curves in Fig. 29. Therefore, we consider the interpolated values in Table VI to be our best estimates of the quadrupole ratios for $W = M_\Delta$.

TABLE VI. Power series for quadrupole ratios in terms of $(W - M_\Delta)$ in units of GeV. The best-fit estimate of the quadrupole ratios at $W = M_\Delta = 1.232$ GeV is given for each analysis method by a_0.

Method	EMR			SMR		
	a_0	a_1	a_2	a_0	a_1	a_2
Legendre	-1.76 ± 0.19	-3.77	-793	-5.87 ± 0.20	53.2	618
Multipole	-2.87 ± 0.19	-13.3	-450	-6.61 ± 0.18	39.3	749

D. Relationship between G_{En} and R_{SM}

Buchmann [77] has derived a relationship

$$R_{SM} = \frac{q M_N}{2Q^2} \frac{G_{En}}{G_{Mn}} \tag{38}$$

between R_{SM} for the $N \to \Delta$ transition and the neutron electric and magnetic Sachs form factors, G_{En} and G_{Mn}. Here q is virtual photon momentum in the c.m. frame. Deviations from this relationship were attributed to three-quark and higher-order currents and were estimated to be at the level of $1/N_c^2$, or about 10%. Figure 30 compares this prediction with recent data [14,17–19] where the band is based upon fitted neutron form factors from Ref. [78]. Note that the growth of the band for $Q^2 > 1.5\,(\mathrm{GeV}/c)^2$, where G_{En} data are presently unavailable, is artificially limited by the use of a model with only two parameters. The Buchmann formula underestimates most of the R_{SM} data. The discrepancy of about 15% at $Q^2 = 1\,(\mathrm{GeV}/c)^2$ is similar to the estimated theoretical uncertainty, but this model predicts a nearly constant quadrupole ratio for larger Q^2 while the data show a steep slope. Note that for the high-Q^2 data, we chose the effective Lagrangian analysis instead of the Legendre analysis from Ref. [19] because truncation errors in the Legendre method are expected to increase with Q^2 [74] and the effective Lagrangian results are consistent with the MAID and DMT analyses of the same data [72]. Although the R_{SM} slope is described well

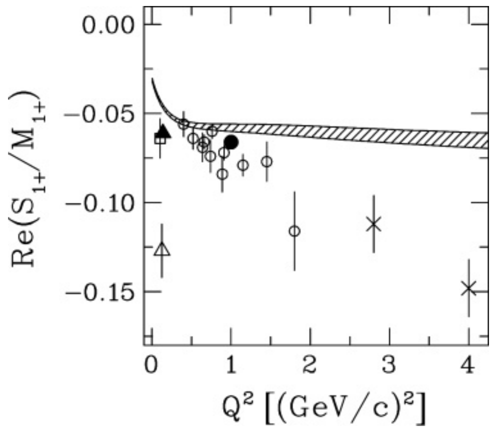

FIG. 30. Comparison between $R_{\rm SM}$ data and Buchmann's formula (band) using fitted neutron form factors. Data: open square [14], filled triangle [17], open triangle [21], open circles [18], crosses [19]; the filled circle is the present result. Small horizontal displacements are used to reduce clutter. Error bars include statistical and systematic but not model uncertainties.

by dynamic models of πN rescattering, perturbative QCD predicts that $R_{\rm SM}$ should become constant asymptotically. Therefore, it would be of interest to extend measurements of G_{En} to higher Q^2 and to use model-independent multipole analysis of new polarization data for pion electroproduction to verify the apparent slope in $R_{\rm SM}$.

E. Sensitivity of Legendre coefficients to specific multipole amplitudes

Even though *sp* truncation and M_{1+} dominance are not sufficiently accurate for quantitative analysis of the quadrupole ratios, that truncation can still provide qualitative insight into the sensitivity of selected Legendre coefficients to particular multipole amplitudes. For example, we note that $A_0^{TTt} \approx 3{\rm Im}M_{1+}^* M_{1-}$, while Fig. 24 shows that most models predict that M_{1-} is nearly real and varies slowly over this range of W. Consequently, one expects the W dependence of A_0^{TTt} to strongly resemble ${\rm Im}M_{1+}$ and its amplitude to be proportional to ${\rm Re}M_{1-}$ and opposite in sign. Figure 31 shows that these expectations are realized by the Legendre fit. The observation that the A_0^{TTt} data are smaller than SAID, larger than DMT and SL, and in good agreement with MAID2003 predictions is consistent with the same pattern seen in Fig. 24 for ${\rm Re}M_{1-}$ and with response function figures in Sec. VI A. A similar correspondence is also observed for A_1^{L+Tn}, but the truncation is not as reliable because Rosenbluth separation is not available and model calculations have greater shape differences. The ${\rm Re}M_{1-}$ amplitude also appears in A_1^{TTn} but is again diluted. Therefore, the best sensitivity to ${\rm Re}M_{1-}$ is provided by the R_{TT}^t response function.

Similarly, model calculations suggest that S_{1-} also varies relatively slowly and is nearly real in this W range, although neither feature is quite as accurate as for M_{1-}. Study of truncated multipole expansions of Legendre coefficients suggests that the best sensitivity to ${\rm Re}S_{1-}$ is offered by the R_{LT}^n response function through its A_0^{LTn} Legendre coefficient. The

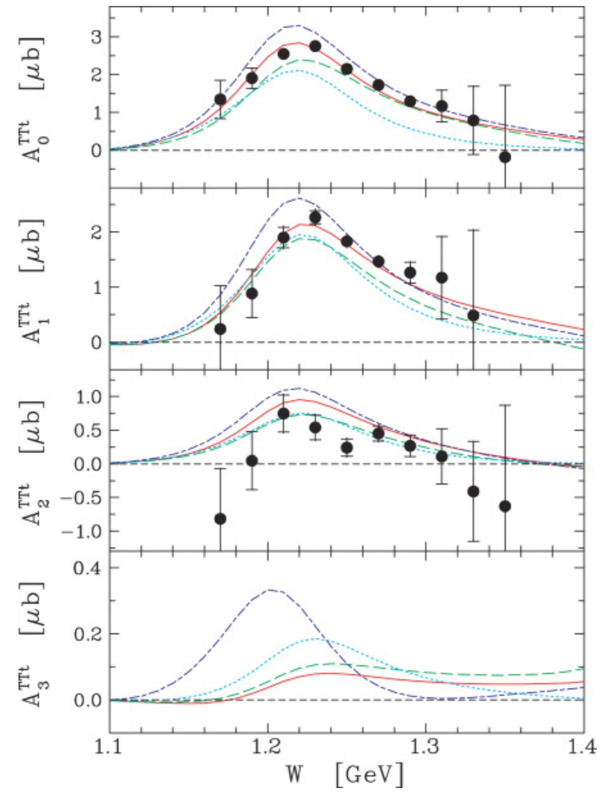

FIG. 31. (Color online) Fitted Legendre coefficients for R_{TT}^t are compared with MAID2003 (red solid), DMT (green dashed), SAID (blue dash-dotted), and SL (cyan dotted). In the simplest approximation, the first and second panels are $-3{\rm Re}M_{1-}{\rm Im}M_{1+}$ and $3{\rm Re}E_{0+}{\rm Im}M_{1+}$, respectively. Inner error bars with end caps are statistical; outer error bars without end caps include systematic uncertainties.

shape differences show that M_{1+} dominance is not as accurate for this Legendre coefficient, but Fig. 32 shows that its W dependence does resemble that of ${\rm Im}M_{1+}$ nonetheless. Thus, we find that the SAID prediction for A_0^{LTn} is considerably too strong while those of MAID2003, DMT, and SL are too weak and that the same pattern is observed in Fig. 24 for ${\rm Re}S_{1-}$.

Within the truncated Legendre expansion, ${\rm Re}E_{0+}$ is isolated by A_0^{TTn}, $A_0^{TT\ell}$, or A_1^{TTt}, which should be equal modulo signs if E_{0+} were real and M_{1+} dominance accurate. The A_1^{TTt} coefficient is included in Fig. 31, but the other figures are omitted and can be found in Ref. [61]. We do observe the expected pattern of signs, and all are similar in shape to ${\rm Im}M_{1+}$, but their magnitudes do not conform to these simplistic predictions. Nevertheless, the relationships between data and model calculations for the Legendre coefficients are similar to those for ${\rm Re}E_{0+}$.

The most complicated situation is S_{0+} because both model predictions and fitted amplitudes show important imaginary contributions to this nonresonant partial wave. Hence, measurement of S_{0+} amplitudes requires LT response functions of both R and I types. The S_{0+} contributions to the truncated Legendre expansion are isolated by 5 R-type and 5 I-type coefficients, but although each group displays a relatively uniform shape with respect to W, there are significant

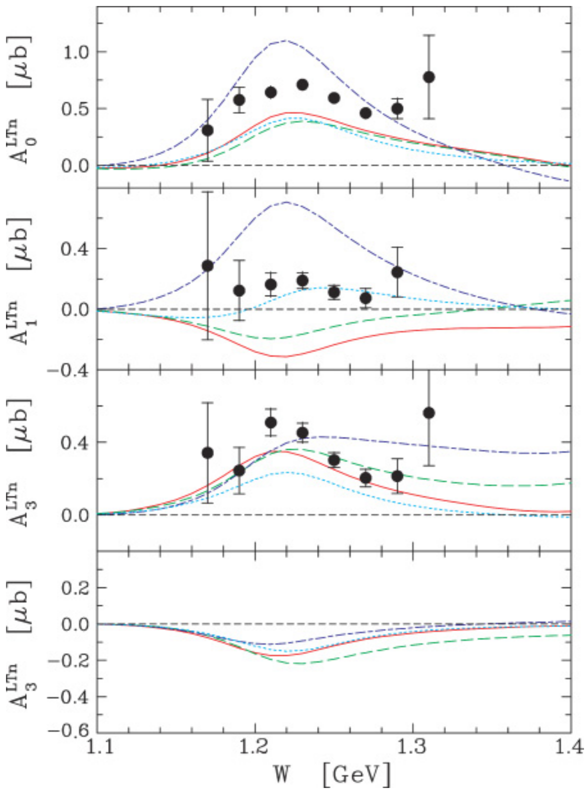

FIG. 32. (Color online) Fitted Legendre coefficients for R_{LT}^n are compared with MAID2003 (red solid), DMT (green dashed), SAID (blue dash-dotted), and SL (cyan dotted). In the simplest approximation, the top panel is $\mathrm{Re}S_{1-}\mathrm{Im}M_{1+}$ and the second is $\mathrm{Im}S_{0+}^{*}M_{1+}$. Inner error bars with end caps are statistical; outer error bars without end caps include systematic uncertainties.

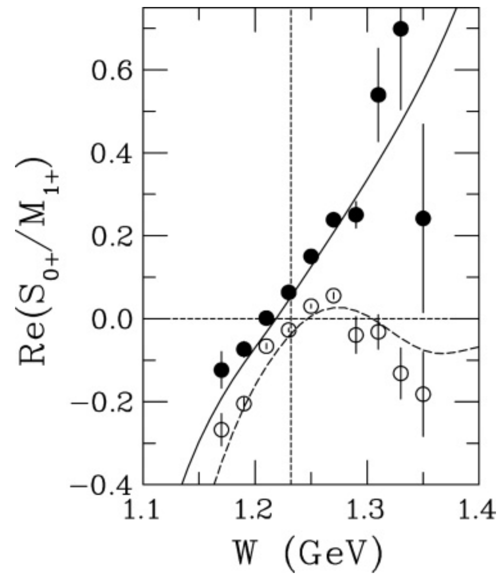

FIG. 33. Comparison between multipole and Legendre analyses of $\mathrm{Re}(S_{0+}/M_{1+})$. Solid and dashed curves show MAID2003 calculations using multipole amplitudes or Legendre coefficients, respectively. Solid (open) circles show experimental ratios based upon multipole (Legendre) fits. The vertical dashed line indicates $W = 1.232$ GeV.

differences in detail that show that the simple truncation is not especially accurate for these coefficients. Nevertheless, the fitted multipole amplitudes provide good fits to all of the LT response functions simultaneously. Therefore, polarization data provide the phase of S_{0+}.

Schmieden [22] speculated that the disagreement between SMR values for $Q^2 \sim 0.13\,(\mathrm{GeV}/c)^2$ obtained by Kalleicher *et al.* [21] using the forward pions and those obtained using cross sections [15] or polarizations [14,23] for forward protons might be explained using $\mathrm{Re}(S_{0+}/M_{1+}) \approx -0.14$. However, recent models predict smaller positive values with relatively slow Q^2 dependence that are similar to $-R_{\mathrm{SM}}$. Although it might appear that one could estimate this quantity using

$$\mathrm{Re}\frac{S_{0+}}{M_{1+}} \approx \frac{2A_0^{LT}}{A_0^T} \approx \frac{2A_0^{LT}}{A_0^{L+T}}, \tag{39}$$

based upon M_{1+} dominance and sp truncation, Fig. 6 shows that A_0^{LT} has a node near M_Δ and is very small for larger W. By contrast, A_1^{LT} peaks near M_Δ. Thus, it is likely that truncation errors in the multipole expansion of Legendre coefficients will be more serious for S_{0+} than for S_{1+}. This problem is illustrated in Fig. 33 which compares fitted values for $\mathrm{Re}(S_{0+}/M_{1+})$ from the multipole analysis with those based upon Eq. (39) where, because Rosenbluth separation is unavailable, we assume that $A_0^T \approx A_0^{L+T}$ because M_{1+} dominance predicts $A_0^L = 0$. We also show MAID2003 calculations for both quantities. We find that MAID2003 describes both the steep slope in $\mathrm{Re}(S_{0+}/M_{1+})$ and the more complicated shape of $2A_0^{LT}/A_0^{L+T}$ fairly well, but these quantities are rather different even in the immediate vicinity of $W = M_\Delta$—the Legendre analysis does not even give the correct sign for this multipole ratio at $W = 1.232$ GeV. The sign difference between these quantities using MAID2003 calculations for $Q^2 = 1\,(\mathrm{GeV}/c)^2$ was previously noted in Ref. [74], and here the same problem is observed in data. The analysis of a recent experiment for $Q^2 = 0.2\,(\mathrm{GeV}/c)^2$ that measured left-right cross section asymmetries for $\theta_\pi = 20^\circ$ and 160° also observed a large difference between ratios based upon M_{1+} dominance and sp truncation and those obtained by scaling MAID2003 S_{0+} and S_{1+} multipoles to fit the data [79]. With a much more complete data set, our multipole analysis does not rely upon models like MAID and gives $\mathrm{Re}(S_{0+}/M_{1+}) = (6.4 \pm 0.7)\%$ at $(W, Q^2) = (1.23, 1.0)$ directly. Assuming that $\mathrm{Re}M_{1+} \approx 0$ for $W \approx M_\Delta$, the ratio $\mathrm{Re}(S_{0+}/M_{1+}) \approx \mathrm{Im}S_{0+}/\mathrm{Im}M_{1+}$ shows that $\mathrm{Im}S_{0+}$ is positive and somewhat larger than the MAID2003 prediction for $W = 1.23$ GeV, as shown in Fig. 23. Although there is nothing special about M_Δ for S_{0+}, we can use the observed slope to estimate $\mathrm{Re}(S_{0+}/M_{1+}) = (7.1 \pm 0.8)\%$ at $(W, Q^2) = (1.232, 1.0)$ for comparison with similar analyses purportedly at $W = M_\Delta$; however, the energy dependence is steep enough that kinematic uncertainties could become important. Recognizing that the Q^2 dependence is mild in most models, neither the present result nor that of Ref. [79] supports Schmieden's hypothesis of a large negative value for this ratio.

TABLE VII. χ_ν^2 for Legendre and multipole analyses.

W (GeV)	χ_ν^2, Legendre	χ_ν^2, multipole
1.17	1.32	1.24
1.19	1.69	1.67
1.21	1.32	1.39
1.23	1.50	1.65
1.25	1.87	1.94
1.27	1.59	1.58
1.29	1.53	1.52
1.31	1.61	1.42
1.33	1.53	1.32
1.35	1.41	1.30

F. Interpretation of χ_ν^2

The Legendre and multipole analyses employ data for differential cross section, beam analyzing power, and recoil polarization response functions with uncertainties that are primarily statistical. The cross section data include uncertainties in acceptance that can also be considered statistical because they are estimated from the flatness of a yield/simulation plateau. The uncertainties for recoil polarization response functions are based upon diagonal elements of the covariance matrix for the maximum likelihood method. However, the fact that reduced chi-square values χ_ν^2 are consistently larger than unity for both Legendre and multipole analyses suggests that uncertainties in extracted quantities may be underestimated. These statistics are listed in Table VII for each W. There are several possible explanations for this observation. First, the various recoil polarization response functions in a given (x, W, Q^2) bin are correlated with each other, but those correlations are not considered by the Legendre or multipole analyses because we have no efficient means to account for them. Thus, the same fluctuation can affect several data points and artificially increase its contribution to χ^2 without necessarily affecting the quality of the fit. Second, systematic uncertainties that vary between kinematic bins were not included in the uncertainties that were used in the Legendre and multipole analyses because their effects upon various response functions are also highly correlated. Third, inaccuracies in baseline calculations of fixed amplitudes would impose a lower limit on χ^2 even if all experimental correlations could be handled properly. Finally, no corrections have been made for polarized radiative corrections.

Radiative corrections for the beam asymmetry in the $p(\vec{e}, e'p)\pi^0$ reaction have been evaluated for $Q^2 = 0.4\,(\mathrm{GeV}/c)^2$ by Afanasev *et al.* [80] and found to be quite small across the $\Delta(1232)$ resonance. Radiative corrections for polarized target asymmetries are presently under investigation and generally appear to be small also [81], but procedures for recoil polarization are not yet available in a form suitable for the present analysis. In principle, external radiation permits additional kinematic dependencies that cannot be accommodated by the response function expansions given in Eq. (3). Analysis of such effects probably requires an iterative procedure that begins with the current results to obtain model response functions, then calculates radiatively corrected polarizations for each experimental event as input to an extended version of the likelihood analysis that would use a more general representation of the ϕ dependence. In the future, it may be possible to improve upon the current multipole results by iteration within a model of radiative corrections and hopefully reduce χ_ν^2, but that is obviously a very ambitious project.

The simplest method of correcting for underestimates of experimental uncertainties is to multiply the uncertainties in extracted quantities by $\sqrt{\chi_\nu^2}$. We have not performed that operation here because it is somewhat arbitrary, assuming that neglected errors are random and uniform, but we provide Table VII for the user's convenience. However, if that procedure is applied, the systematic uncertainties should probably be reduced to avoid double-counting of random errors presently labeled systematic.

VIII. SUMMARY AND CONCLUSIONS

We measured angular distributions for differential cross section, beam analyzing power, and recoil polarization in the $p(\vec{e}, e'\vec{p})\pi^0$ reaction at $Q^2 = 1\,(\mathrm{GeV}/c)^2$ with $1.17 \leqslant W \leqslant 1.35$ GeV across the Δ resonance and obtained 14 separated response functions and two Rosenbluth combinations, of which 12 have been measured for the first time.

We compared the data for response functions with calculations for four recent models: MAID, DMT, SAID, and SL. Variations among these models are relatively small at $W \approx M_\Delta$ for quantities that depend upon real parts of interference products but increase with W. Variations among models are much larger for quantities dependent upon imaginary parts that are more sensitive to background amplitudes. MAID and DMT are similar and in relatively good agreement with data for $W \approx M_\Delta$, but neither provides a uniformly good description of the data for larger W. The SL model, which does not include higher resonances, underpredicts the cross section for larger W, while DMT is too strong. The SAID model has considerable difficulty with helicity-independent LT response functions that are probably caused mostly by its rather strong $\mathrm{Re}S_{1-}$ amplitude.

We performed a multipole analysis that fits both real and imaginary parts of the multipole amplitudes for low partial waves, while those for higher partial waves are constrained either by Born terms or by the best available model calculations. Fitted multipole amplitudes based upon Born, MAID, DMT, or SL models are practically indistinguishable, but the available version of SAID does not provide a suitable baseline because some of its $\ell_\pi \geqslant 2$ amplitudes are too strong. The final analysis is based upon the Born model to minimize bias. We chose not to vary $\mathrm{Im}M_{1-}$ in the final analysis because it is predicted to be negligible in our energy range but its fitted values are strongly correlated with those of $\mathrm{Im}S_{1-}$ for the present data set. We were able to extract consistent results for all $\ell_\pi \leqslant 1$ amplitudes, except $\mathrm{Im}M_{1-}$, plus the real parts of $2-$ multipoles. The most significant differences between fitted and model amplitudes are found in $0+$ and $1-$ multipoles. The data also show that $\mathrm{Im}S_{0+}$ grows faster than predicted by MAID, DMT, or SL, but it is described reasonably well by SAID. Good sensitivity to $\mathrm{Re}M_{1-}$ is provided by the R_{TT}^{t} response function; there is a wide spread among models, but MAID2003 fits the ReM_{1-} data best and is close to the Born baseline. Similarly, the best sensitivity to ReS_{1-} is provided by R^n_{LT}, but none of the models are accurate—SAID is much too strong while MAID, DMT, and SL are too weak for that amplitude. The data are substantially stronger than the Born amplitude, suggesting significant longitudinal Roper contributions arising from a radial excitation.

We find that truncation errors in the traditional Legendre analysis of $N \to \Delta$ quadrupole ratios can be significantly larger than statistical errors. Using parabolic fits to the energy dependence, we obtain $\tilde{R}^{(p\pi^0)}_{\rm SM} = (-5.87 \pm 0.20)\%$ and $\tilde{R}^{(p\pi^0)}_{\rm EM} = (-1.76 \pm 0.19)\%$ from the traditional analysis or $R^{(p\pi^0)}_{\rm SM} = (-6.61 \pm 0.18)\%$ and $R^{(p\pi^0)}_{\rm EM} = (-2.87 \pm 0.19)\%$ from the multipole analysis for $W = 1.232$ GeV and $Q^2 = 1.0\,({\rm GeV}/c)^2$. These results are consistent with the single-energy analysis published previously [33]. The model dependence of the multipole analysis is small, and the Legendre fits are stable with respect to the number of fitted terms, yet the differences between these analyses are several standard deviations. We have demonstrated that the multipole analysis is more reliable because it does not depend upon M_{1+} dominance or sp truncation. Both model calculations and the multipole analysis of data demonstrate that neither assumption is reliable and that multipole products omitted by that truncation scheme make important contributions to the Legendre coefficients that spoil the accuracy of the simple estimators of quadrupole ratios employed by the traditional Legendre analysis. Truncation errors are especially severe for $\tilde{R}_{\rm EM}$.

We also find that ${\rm Re}(S_{0+}/M_{1+}) = (7.1 \pm 0.8)\%$ at $W = 1.232$ GeV is qualitatively consistent with most recent models and with a recent measurement [79] at $Q^2 = 0.2\,({\rm GeV}/c)^2$ of left-right cross section asymmetries at a pair of supplementary proton angles, but it is inconsistent with a recent hypothesis [22] that a large negative value is needed to explain inconsistencies between SMR analyses at $Q^2 = 0.13\,({\rm GeV}/c)^2$ using earlier data for forward versus backward θ_π. Truncation errors in the Legendre estimator for ${\rm Re}(S_{0+}/M_{1+})$ are quite severe [74], even resulting in an incorrect sign at $Q^2 \sim 1\,({\rm GeV}/c)^2$. The analysis in Ref. [79] relied on the MAID model instead of the Legendre estimator, but accurate, model-independent results require a phase-sensitive multipole analysis as performed here.

In conclusion, recoil and/or target polarization data are essential to multipole analyses of meson electroproduction reactions, providing access to the relative phase between resonant and nonresonant contributions. Although neutral pion electroproduction in the Δ region is the easiest example, this experiment demonstrates the feasibility of the method, and we hope that it will be applied over wider kinematic ranges and to related reactions. An advantage of this type of analysis is that it minimizes the dependence upon models; however, it does not guarantee that the fitted multipole amplitudes will depend smoothly on both W and Q^2. Model-dependent analyses which adjust parameters of an effective Lagrangian or unitary isobar model should produce kinematically smooth multipole amplitudes at the expense of possible bias. Presumably, analyses of these types would also be less sensitive to variations of acceptance-averaged W and Q^2 between bins of the angular variables (x, ϕ). Both types of analyses would benefit from more extensive coverage in W. With sufficient kinematic coverage one hopes to obtain reliable transition form factors for overlapping resonances.

ACKNOWLEDGMENTS

We thank Dr. L. Tiator for MAID and DMT multipole amplitudes, Dr. T.-S. H. Lee for SL multipole amplitudes, Dr. R. Arndt for SAID subroutines, and Dr. I. Aznauryan for discussions of the unitary isobar model. Finally, we thank Dr. T. Payerle for the first version of EPIPROD. This work was supported by DOE Contract No. DE-AC05-84ER40150 Modification No. M175 under which the Southeastern Universities Research Association (SURA) operates the Thomas Jefferson National Accelerator Facility. We acknowledge additional grants from the U.S. DOE and NSF, Canadian NSERC, Italian INFN, French CNRS and CEA, and Swedish VR.

APPENDIX: BORN BASELINE MODEL

In this Appendix, we summarize the Born baseline model used for the multipole analysis, including only the terms that contribute to the $p\pi^0$ channel. The electromagnetic vertices are represented by effective Lagrangians of the form

$$\mathcal{L}_{\gamma NN} = -e\bar{N}\left[F_1(Q^2)\gamma_\mu \mathcal{A}^\mu + F_2(Q^2)\frac{\sigma_{\mu\nu}}{2m_N}(\partial^\mu \mathcal{A}^\nu)\right]N, \tag{A1a}$$

$$\mathcal{L}_{\gamma\pi V} = e\frac{\lambda_V}{m_\pi}\varepsilon_{\mu\nu\alpha\beta}(\partial^\mu A^\nu)\pi_3\partial^\alpha\left(\delta_{i,3}\omega^\beta + \rho_i^\beta\right)F_{\gamma\pi V}(Q^2), \tag{A1b}$$

where N represents a nucleon field operator, A^μ is the electromagnetic vector potential, $\boldsymbol{\pi}$ is the pion field as an isospin vector, and $V \in \{\omega, \rho\}$ denotes a vector meson. We used conventional dipole and Galster form factors for the nucleon and monopole form factors

$$F_{\gamma\pi V}(Q^2) = \left(1 + \frac{Q^2}{m_V^2}\right)^{-1} \tag{A2}$$

for $\gamma\pi V$ vertices. The $\gamma\pi V$ and VNN parameters are listed in Table VIII and were taken from Ref. [67].

We used pure pseudovector πNN coupling

$$\mathcal{L}_{\pi NN} = -\frac{g^{PV}_{\pi NN}}{2m_N}\bar{N}\gamma_5\gamma_\mu\boldsymbol{\tau}\cdot(\partial^\mu\boldsymbol{\pi})N, \tag{A3}$$

with $g^{PV}_{\pi NN} = 13.4$. Drechsel *et al.* [67] proposed a more flexible πNN model that interpolates between pseudovector coupling for small p_π and pseudoscalar coupling for large p_π, but this variation only affects real parts of 0+ and 1− baseline

TABLE VIII. Parameters for vector-meson vertices.

V	m_V (MeV)	g_{V_1}	g_{V_2}	Λ_{VNN} (MeV)	λ_V
ω	782.6	21	−12	1200	0.314
ρ	769.0	2	13	1500	0.103

multipoles, and the fitted parameters simply compensate for variations of the pseudoscalar/pseudovector mixture anyway.

Finally, the VNN coupling is described by

$$\mathcal{L}_{VNN} = -\bar{N}\left[\left(g_{V_1}\gamma_\mu + \frac{g_{V_2}}{2m_N}\sigma_{\mu\nu}\partial^\mu\right)(\omega^\nu + \boldsymbol{\tau}\cdot\boldsymbol{\rho}^\nu)\right] \times N F_{VNN}(t), \tag{A4}$$

where ω^ν and $\boldsymbol{\rho}^\nu$ represent ω and ρ fields. A strong form factor,

$$F_{VNN}(t) = \frac{\Lambda_{VNN}^2 - m_V^2}{\Lambda_{VNN}^2 - t}, \tag{A5}$$

is applied to the VNN vertex according to the prescription of Brown *et al.* [82].

[1] S. Capstick and W. Roberts, Prog. Part. Nucl. Phys. **45**, S241 (2000).
[2] Z. Li, Phys. Rev. D **44**, 2841 (1991).
[3] Z. Li, V. Burkert, and Z. Li, Phys. Rev. D **46**, 70 (1991).
[4] S. L. Glashow, Physica (Utrecht) **96A**, 27 (1979).
[5] N. Isgur, G. Karl, and R. Koniuk, Phys. Rev. D **25**, 2394 (1982).
[6] U. Meyer, E. Hernández, and A. J. Buchmann, Phys. Rev. C **64**, 035203 (2001).
[7] S. S. Kamalov and S. N. Yang, Phys. Rev. Lett. **83**, 4494 (1999).
[8] M. Fiolhais, G. Golli, and S. Sirca, Phys. Lett. **B373**, 229 (1996).
[9] A. J. Buchmann and E. M. Henley, Phys. Rev. C **63**, 015202 (2001).
[10] C. N. Papanicolas, in *Proceedings of the Workshop on the Physics of Excited Nucleons—NSTAR2001*, edited by D. Drechsel and L. Tiator (World Scientific, Singapore, 2001), p. 11.
[11] G. Blanpied *et al.*, Phys. Rev. Lett. **79**, 4337 (1997).
[12] R. Beck *et al.*, Phys. Rev. C **61**, 035204 (2000).
[13] R. A. Arndt, W. J. Briscoe, I. I. Strakovsky, and R. L. Workman, Phys. Rev. C **66**, 055213 (2002).
[14] T. Pospischil *et al.*, Phys. Rev. Lett. **86**, 2959 (2001).
[15] C. Mertz *et al.*, Phys. Rev. Lett. **86**, 2963 (2001).
[16] C. Kunz *et al.*, Phys. Lett. **B564**, 21 (2003).
[17] N. F. Sparveris *et al.*, Phys. Rev. Lett. **94**, 022003 (2005).
[18] K. Joo *et al.*, Phys. Rev. Lett. **88**, 122001 (2002).
[19] V. V. Frolov *et al.*, Phys. Rev. Lett. **82**, 45 (1999).
[20] G. Laveissière *et al.*, Phys. Rev. C **69**, 045203 (2004).
[21] F. Kalleicher, U. Dittmayer, R. W. Gothe, H. Putsche, T. Reichelt, B. Schoch, and M. Wilhelm, Z. Phys. A **359**, 201 (1997).
[22] H. Schmieden, in *Proceedings of the Workshop on the Physics of Excited Nucleons—NSTAR 2001*, edited by D. Drechsel and L. Tiator (World Scientific, Singapore, 2001), p. 27.
[23] G. A. Warren *et al.*, Phys. Rev. C **58**, 3722 (1998).
[24] P. Bartsch *et al.*, Phys. Rev. Lett. **88**, 142001 (2002).
[25] K. Joo *et al.*, Phys. Rev. C **68**, 032201 (2003).
[26] N. F. Sparveris *et al.*, Phys. Rev. C **67**, 058201 (2003).
[27] A. S. Raskin and T. W. Donnelly, Ann. Phys. (NY) **191**, 78 (1989).
[28] R. W. Lourie, Nucl. Phys. **A509**, 653 (1990).
[29] R. W. Lourie, Z. Phys. C **50**, 345 (1991).
[30] H. Schmieden, Eur. Phys. J. A **1**, 427 (1998).
[31] A. Biselli *et al.*, Phys. Rev. C **68**, 035202 (2003).
[32] R. D. Vita *et al.*, Phys. Rev. Lett. **88**, 082001 (2002).
[33] J. J. Kelly *et al.*, Phys. Rev. Lett. **95**, 102001 (2005).
[34] J. J. Kelly, Phys. Rev. C **60**, 054611 (1999).
[35] H. Schmieden and L. Tiator, Eur. Phys. J. A **8**, 15 (2000).
[36] J. Alcorn *et al.*, Nucl. Instrum. Methods A **522**, 294 (2004).
[37] V. Punjabi *et al.*, Phys. Rev. C **71**, 055202 (2005).
[38] R. E. Roché, Ph.D. thesis, Florida State University, 2003.
[39] Z. Chai, Ph.D. thesis, Massachusetts Institute of Technology, 2003.
[40] S. Escoffier, Ph.D. thesis, University of Paris, 2001.
[41] J. M. Grames *et al.*, Phys. Rev. ST Accel. Beams **7**, 042802 (2004).
[42] K. G. Fissum *et al.*, Nucl. Instrum. Methods A **474**, 108 (2001).
[43] K. L. Brown, Technical Report 91, SLAC, 1979 (unpublished).
[44] V. L. Rvachev, *Theory of R-functions and Some Applications* (Naukova Dumka, Kiev, Ukraine, 1982), in Russian.
[45] V. L. Rvachev and T. I. Sheiko, Appl. Mech. Rev. **48**, 151 (1995).
[46] M. M. Rvachev, Ph.D. thesis, Massachusetts Institute of Technology, 2003.
[47] M. M. Rvachev *et al.*, Phys. Rev. Lett. **94**, 192302 (2005).
[48] P. E. Ulmer, www.physics.odu.edu/~ulmer/mceep/mceep.html.
[49] D. Drechsel, O. Hanstein, S. S. Kamalov, L. Tiator, and S. N. Yang, www.kph.uni-mainz.de/MAID.
[50] E. Borie and D. Drechsel, Nucl. Phys. **A167**, 369 (1971).
[51] M. K. Jones (2000), www.physics.umd.edu/enp/jjkelly/e91011/Reports/Analysis/report_on_deadtime.ps.gz.
[52] L. C. Smith *et al.* (2002), planck.phys.virginia.edu/~lcs1h/clas.
[53] D. Besset, B. Favier, L. G. Greeniaus, R. Hess, C. Lechanoine, D. Rapin, and D. W. Werren, Nucl. Instrum. Methods **166**, 515 (1979).
[54] M. W. McNaughton *et al.*, Nucl. Instrum. Methods A **241**, 435 (1985).
[55] M. K. Jones *et al.*, Phys. Rev. Lett. **84**, 1398 (2000).
[56] O. Gayou *et al.*, Phys. Rev. Lett. **88**, 092301 (2002).
[57] E. J. Brash, A. Kozlov, S. Li, and G. M. Huber, Phys. Rev. C **65**, 051001(R) (2002).
[58] J. J. Kelly and O. Gayou (2005), www.physics.umd.edu/enp/jjkelly/e91011/Reports/Analysis/pseudodata_analysis. ps.gz.
[59] L. Pentchev, JLAB-TN-03-024 (2003).
[60] T. Sato and T.-S. H. Lee, Phys. Rev. C **63**, 055201 (2001).
[61] J. J. Kelly (2005), www.physics.umd.edu/enp/jjkelly/e91011/Reports/Analysis/legendre.ps.gz.
[62] J. J. Kelly (2005), www.physics.umd.edu/enp/jjkelly/e91011/Reports/Analysis/mpfit.ps.gz.
[63] V. D. Burkert and T.-S. H. Lee, Int. J. Mod. Phys. E **13**, 1035 (2004).
[64] R. A. Arndt, R. L. Workman, Z. Li, and L. D. Roper, Phys. Rev. C **42**, 1853 (1990).
[65] K. M. Watson, Phys. Rev. **95**, 228 (1954).
[66] R. A. Arndt, W. J. Briscoe, I. I. Strakovsky, and R. L. Workman, in *Proceedings of the Workshop on the Physics of Excited Nucleons—NSTAR2002*, edited by S. A. Dytman and E. S. Swanson (World Scientific, Singapore, 2003), p. 234.
[67] D. Drechsel, O. Hanstein, S. S. Kamalov, and L. Tiator, Nucl. Phys. **A645**, 145 (1999).
[68] D. Drechsel, O. Hanstein, S. S. Kamalov, L. Tiator, and S. N. Yang, www.kph.uni-mainz.de/maid/maid2003.
[69] L. Tiator, D. Drechsel, S. Kamalov, M. M. Giannini, E. Santopinto, and A. Vassalo, Eur. Phys. J. A **19**, s01, 55 (2004).

[70] J. C. Alder *et al*., Nucl. Phys. B **46**, 573 (1972).
[71] A. Latham *et al*., Nucl. Phys. B **189**, 1 (1981).
[72] S. S. Kamalov, S. N. Yang, D. Drechsel, O. Hanstein, and L. Tiator, Phys. Rev. C **64**, 032201(R) (2001).
[73] D. Drechsel, O. Hanstein, S. S. Kamalov, L. Tiator, and S. N. Yang, www.kph.uni-mainz.de/maid/dmt.
[74] J. J. Kelly, Phys. Rev. C **72**, 048201 (2005).
[75] J. J. Kelly and T. M. Payerle, www.physics.umd.edu/enp/jjkelly/EPIPROD.
[76] R. A. Arndt, W. J. Briscoe, R. L. Workman, and I. I. Strakovsky, gwdac.phys.gwu.edu.
[77] A. J. Buchmann, Phys. Rev. Lett. **93**, 212301 (2004).
[78] J. J. Kelly, Phys. Rev. C **70**, 068202 (2004).
[79] D. Elsner *et al*., Eur. Phys. J. A **27**, 91 (2006).
[80] A. Afanasev, I. Akushevich, V. Burkert, and K. Joo, Phys. Rev. D **66**, 074004 (2002).
[81] A. Afanasev (private communication, 2005).
[82] G. E. Brown, M. Rho, and W. Weise, Nucl. Phys. **A454**, 669 (1986).
[83] See EPAPS Document No. E-PRVCAN-75-023702 for tables of data, Legendre coefficients, and multipole amplitudes. We also include the three internal reports [58,61,62] cited in the present article. A direct link to this document may be found in the online article's HTML reference section. The document may also be reached via the EPAPS homepage (http://www.aip.org/pubservs/epaps.html) or from ftp.aip.org in the directory /epaps/. See the EPAPS homepage for more information.